PMC Physics A

PhysMathCentral

Research article

Open Access

Exclusive ρ^0 production in deep inelastic scattering at HERA

ZEUS Collaboration

Email: ZEUS Collaboration - gallo@mail.desy.de

Published: 12 November 2007

PMC Physics A 2007, 1:6 doi:10.1186/1754-0410-1-6

Received: 13 August 2007
Accepted: 12 November 2007

This article is available from: http://www.physmathcentral.com/1754-0410/1/6

© 2007 Zeus Collaboration; This is an Open Access article distributed under the terms of the Creative Commons Attribution License (http://creativecommons.org/licenses/by/2.0), which permits unrestricted use, distribution, and reproduction in any medium, provided the original work is properly cited.

Abstract

Exclusive ρ^0 electroproduction at HERA has been studied with the ZEUS detector using 120 pb^{-1} of integrated luminosity collected during 1996–2000. The analysis was carried out in the kinematic range of photon virtuality $2 < Q^2 < 160$ GeV^2, and $\gamma^* p$ centre-of-mass energy $32 < W < 180$ GeV. The results include the Q^2 and W dependence of the $\gamma^* p \to \rho^0 p$ cross section and the distribution of the squared-four-momentum transfer to the proton. The helicity analysis of the decay-matrix elements of the ρ^0 was used to study the ratio of the $\gamma^* p$ cross section for longitudinal and transverse photon as a function of Q^2 and W. Finally, an effective Pomeron trajectory was extracted. The results are compared to various theoretical predictions.

PACS Codes: 13.60.Hb, 13.60.Le

1 Introduction

Two of the most surprising aspects of high-energy deep inelastic scattering (DIS) observed at the HERA *ep* collider have been the sharp rise of the proton structure function, F_2, with decreasing value of Bjorken x and the abundance of events with a large rapidity gap in the hadronic final state [1]. The latter are identified as due to diffraction in the deep inelastic regime. A contribution to the diffractive cross section arises from the exclusive production of vector mesons (VM).

High-energy exclusive VM production in DIS has been postulated to proceed through two-gluon exchange [2,3], once the scale, usually taken as the virtuality Q^2 of the exchanged photon, is large enough for perturbative Quantum Chromodynamics (pQCD) to be applicable. The gluons in the proton, which lie at the origin of the sharp increase of F_2, are also expected to cause the VM cross section to increase with increasing photon proton centre-of-mass energy, W, with the rate of increase growing with Q^2. Moreover, the effective size of the virtual photon decreases with increasing Q^2, leading to a flatter distribution in t, the four-momentum-transfer squared at

the proton vertex. All these features, with varying levels of significance, have been observed at HERA [4-10] in the exclusive production of ρ^0, ω, ϕ and J/ψ mesons.

This paper reports on an extensive study of the properties of exclusive ρ^0-meson production,

$$\gamma^* p \to \rho^0 p,$$

based on a high statistics data sample collected with the ZEUS detector during the period 1996–2000, corresponding to an integrated luminosity of about 120 pb^{-1}.

2 Theoretical background

Calculations of the VM production cross section in DIS require knowledge of the $q\bar{q}$ wave-function of the virtual photon, specified by QED and which depends on the polarisation of the virtual photon. For longitudinally polarised photons, γ_L^*, $q\bar{q}$ pairs of small transverse size dominate [3]. The opposite holds for transversely polarised photons, γ_T^*, where $q\bar{q}$ configurations with large transverse size dominate. The favourable feature of exclusive VM production is that, at high Q^2, the longitudinal component of the virtual photon is dominant. The interaction cross section in this case can be fully calculated in pQCD [11], with two-gluon exchange as the leading process in the high-energy regime. For heavy vector mesons, such as the J/ψ or the Υ, perturbative calculations apply even at $Q^2 = 0$, as the smallness of the $q\bar{q}$ dipole originating from the photon is guaranteed by the mass of the quarks.

Irrespective of particular calculations [12], in the region dominated by perturbative QCD the following features are predicted:

- the total $\gamma^* p \to Vp$ cross section, $\sigma_{\gamma^* p}$, exhibits a steep rise with W, which can be parameterised as $\sigma \sim W^\delta$, with δ increasing with Q^2;

- the Q^2 dependence of the cross-section, which for a longitudinally polarised photon is expected to behave as Q^{-6}, is moderated to become Q^{-4} by the rapid increase of the gluon density with Q^2;

- the distribution of t becomes universal, with little or no dependence on W or Q^2;

- breaking of the s-channel helicity conservation (SCHC) is expected.

In the region where perturbative calculations are applicable, exclusive vector-meson production could become a complementary source of information on the gluon content of the proton. At present, the following theoretical uncertainties have been identified:

• the calculation of $\sigma(\gamma^* p \to Vp)$ involves the generalised parton distributions [13,14], which are not well tested; in addition [15], it involves gluon densities outside the range constrained by global QCD analyses of parton densities;

• higher-order corrections have not been fully calculated [16]; therefore the overall normalisation is uncertain and the scale at which the gluons are probed is not known;

• the rapid rise of $\sigma_{\gamma^* p}$ with W implies a non-zero real part of the scattering amplitude, which is not known;

• the wave-functions of the vector mesons are not fully known.

In spite of all these problems, precise measurements of differential cross sections separated into longitudinal and transverse components [17], should help to resolve the above theoretical uncertainties.

It is important in these studies to establish a region of phase space where hard interactions dominate over the non-perturbative soft component. If the relative transverse momentum of the $q\bar{q}$ pair is small, the colour dipole is large and perturbative calculations do not apply. In this case the interaction looks similar to hadron-hadron elastic scattering, described by soft Pomeron exchange as in Regge phenomenology [18].

The parameters of the soft Pomeron are known from measurements of total cross sections for hadron-hadron interactions and elastic proton-proton measurements. It is usually assumed that the Pomeron trajectory is linear in t:

$$\alpha_{\mathbb{P}}(t) = \alpha_{\mathbb{P}}(0) + \alpha'_{\mathbb{P}} t. \tag{1}$$

The parameter $\alpha_{\mathbb{P}}(0)$ determines the energy behaviour of the total cross section,

$$\sigma_{\text{tot}} \sim (W^2)^{\alpha_{\mathbb{P}}(0)-1}$$

and $\alpha'_{\mathbb{P}}$ describes the increase of the slope b of the t distribution with increasing W. The value of $\alpha'_{\mathbb{P}}$ is inversely proportional to the square of the typical transverse momenta participating in the

exchanged trajectory. A large value of $\alpha'_{\mathbb{P}}$ suggests the presence of low transverse momenta typical of soft interactions. The accepted values of $\alpha_{\mathbb{P}}(0)$ [19] and $\alpha'_{\mathbb{P}}$ [20] are

$$\alpha_{\mathbb{P}}(0) = 1.096 \pm 0.003$$
$$\alpha'_{\mathbb{P}} = 0.25 \text{ Gev}^{-2}.$$

The non-universality of $\alpha_{\mathbb{P}}(0)$ has been established in inclusive DIS, where the slope of the $\gamma^* p$ total cross section with W has a pronounced Q^2 dependence [21]. The value of $\alpha'_{\mathbb{P}}$ can be determined from exclusive VM production at HERA via the W dependence of the exponential b slope of the t distribution for fixed values of W, where b is expected to behave as

$$b(W) = b_0 + 4\alpha'_{\mathbb{P}} \ln \frac{W}{W_0},$$

where b_0 and W_0 are free parameters. The value of $\alpha'_{\mathbb{P}}$ can also be derived from the W dependence of $d\sigma/dt$ at fixed t,

$$\frac{d\sigma}{dt}(W) = F(t) W^{2[2\alpha_{\mathbb{P}}(t)-2]}, \tag{2}$$

where $F(t)$ is an arbitrary function. This approach has the advantage that no assumption needs to be made about the t dependence. The first indications from measurements of $\alpha_{\mathbb{P}}(t)$ in exclusive J/ψ photoproduction [8,22] are that $\alpha_{\mathbb{P}}(0)$ is larger and $\alpha'_{\mathbb{P}}$ is smaller than those of the above soft Pomeron trajectory.

3 Experimental set-up

The present measurement is based on data taken with the ZEUS detector during two running periods of the HERA *ep* collider. During 1996–1997, protons with energy 820 GeV collided with 27.5 GeV positrons, while during 1998–2000, 920 GeV protons collided with 27.5 GeV electrons or positrons. The sample used for this study corresponds to an integrated luminosity of 118.9 pb^{-1}, consisting of 37.2 pb^{-1} e^+p sample from 1996–1997 and 81.7 pb^{-1} from the 1998–2000 sample (16.7 pb^{-1} e^- and 65.0 pb^{-1} e^+) [1].

A detailed description of the ZEUS detector can be found elsewhere [23,24]. A brief outline of the components that are most relevant for this analysis is given below.

1. From now on, the word "electron" will be used as a generic term for both electrons and positrons.

Charged particles are tracked in the central tracking detector (CTD) [25-27]. The CTD consists of 72 cylindrical drift chamber layers, organised in nine superlayers covering the polar-angle [2] region $15° < \theta < 164°$. The CTD operates in a magnetic field of 1.43 T provided by a thin solenoid. The transverse-momentum resolution for full-length tracks is $\sigma(p_T)/p_T = 0.0058 p_T \oplus 0.0065 \oplus 0.0014/p_T$, with p_T in GeV.

The high-resolution uranium-scintillator calorimeter (CAL) [28-31] covers 99.7% of the total solid angle and consists of three parts: the forward (FCAL), the barrel (BCAL) and the rear (RCAL) calorimeters. Each part is subdivided transversely into towers and longitudinally into one electromagnetic section (EMC) and either one (in RCAL) or two (in BCAL and FCAL) hadronic sections. The CAL energy resolutions, as measured under test-beam conditions, are $\sigma(E)/E = 0.18/\sqrt{E}$ for electrons and $\sigma(E)/E = 0.35/\sqrt{E}$ for hadrons, with E in GeV.

The position of the scattered electron was determined by combining information from the CAL, the small-angle rear tracking detector [32] and the hadron-electron separator [33].

In 1998, the forward plug calorimeter (FPC) [34] was installed in the 20×20 cm^2 beam hole of the FCAL with a small hole of radius 3.15 cm in the centre to accommodate the beam pipe. The FPC increased the forward calorimeter coverage by about one unit in pseudorapidity to $\eta \leq 5$.

The leading-proton spectrometer (LPS) [35] detected positively charged particles scattered at small angles and carrying a substantial fraction, x_L, of the incoming proton momentum; these particles remained in the beam-pipe and their trajectories were measured by a system of silicon microstrip detectors, located between 23.8 m and 90.0 m from the interaction point. The particle deflections induced by the magnets of the proton beam-line allowed a momentum analysis of the scattered proton.

During the 1996–1997 data taking, a proton-remnant tagger (PRT1) was used to tag events in which the proton dissociates. It consisted of two layers of scintillation counters perpendicular to the beam at $Z = 5.15$ m. The two layers were separated by a 2 mm-thick lead absorber. The pseudorapidity range covered by the PRT1 was $4.3 < \eta < 5.8$.

The luminosity was measured from the rate of the bremsstrahlung process $ep \to e\gamma p$. The photon was measured in a lead-scintillator calorimeter [36-38] placed in the HERA tunnel at $Z = -107$ m.

2. The ZEUS coordinate system is a right-handed Cartesian system, with the Z axis pointing in the proton direction, referred to as the "forward direction", and the X axis pointing left towards the centre of HERA. The coordinate origin is at the nominal interaction point.

4 Data selection and reconstruction

The following kinematic variables are used to describe exclusive ρ^0 production and its subsequent decay into a $\pi^+\pi^-$ pair:

- the four-momenta of the incident electron (k), scattered electron (k'), incident proton (P), scattered proton (P') and virtual photon (q);

- $Q^2 = -q^2 = -(k - k')^2$, the negative squared four-momentum of the virtual photon;

- $W^2 = (q + P)^2$, the squared centre-of-mass energy of the photon-proton system;

- $\gamma = (P \cdot q)/(P \cdot k)$, the fraction of the electron energy transferred to the proton in its rest frame;

- $M_{\pi\pi'}$ the invariant mass of the two decay pions;

- $t = (P - P')^2$, the squared four-momentum transfer at the proton vertex;

- three helicity angles, Φ_h, θ_h and ϕ_h (see Section 9).

The kinematic variables were reconstructed using the so-called "constrained" method [10,39], which uses the momenta of the decay particles measured in the CTD and the reconstructed polar and azimuthal angles of the scattered electron.

The online event selection required an electron candidate in the CAL, along with the detection of at least one and not more than six tracks in the CTD.

In the offline selection, the following further requirements were imposed:

- the presence of a scattered electron, with energy in the CAL greater than 10 GeV and with an impact point on the face of the RCAL outside a rectangular area of 26.4×16 cm^2;

- $E - P_Z > 45$ GeV, where $E - P_Z = \sum_i (E_i - p_{Z_i})$ and the summation is over the energies and longitudinal momenta of the final-state electron and pions, was imposed. This cut excludes events with high energy photons radiated in the initial state;

- the Z coordinate of the interaction vertex within ± 50 cm of the nominal interaction point;

- in addition to the scattered electron, exactly two oppositely charged tracks, each associated with the reconstructed vertex, and each having pseudorapidity $|\eta|$ less than 1.75 and transverse

momentum greater than 150 MeV; this excluded regions of low reconstruction efficiency and poor momentum resolution in the CTD. These tracks were treated in the following analysis as a $\pi^+\pi^-$ pair;

• events with any energy deposit larger than 300 MeV in the CAL and not associated with the pion tracks (so-called 'unmatched islands') were rejected [40-42].

In addition, the following requirements were applied to select kinematic regions of high acceptance:

• the analysis was restricted to the kinematic regions $2 < Q^2 < 80$ GeV^2 and $32 < W < 160$ GeV in the 1996–1997 data and $2 < Q^2 < 160$ GeV^2 and $32 < W < 180$ GeV in the 1998–2000 sample;

• only events in the $\pi^+\pi^-$ mass interval $0.65 < M_{\pi\pi} < 1.1$ GeV and with $|t| < 1$ GeV^2 were taken. The mass interval is slightly narrower than that used previously [10], in order to reduce the effect of the background from non-resonant $\pi^+\pi^-$ production. In the selected $M_{\pi\pi}$ range, the resonant contribution is ≈ 100% (see Section 8).

The above selection yielded 22,400 events in the 1996–1997 sample and 49,300 events in the 1998–2000 sample, giving a total of 71,700 events for this analysis.

5 Monte Carlo simulation

The relevant Monte Carlo (MC) generators have been described in detail previously [10]. Here their main features are summarised.

The program ZEUSVM [43] interfaced to HERACLES4.4 [44] was used. The effective Q^2, W and t dependences of the cross section were parameterised to reproduce the data [42].

The decay angular distributions were generated uniformly and the MC events were then iteratively reweighted using the results of the present analysis for the 15 combinations of matrix elements r^{04}_{ik}, r^{α}_{ik} (see Section 9).

The contribution of the proton-dissociative process was studied with the EPSOFT [45] generator for the 1996–1997 data and with PYTHIA [46] for the 1998–2000 data. The Q^2, W and t dependences were parameterised to reproduce the control samples in the data. The decay angular distributions were generated as in the ZEUSVM sample.

The generated events were processed through the same chain of selection and reconstruction procedures as the data, thus accounting for trigger as well as detector acceptance and smearing effects. For both MC sets, the number of simulated events after reconstruction was about a factor of seven greater than the number of reconstructed data events.

All measured distributions are well described by the MC simulations. Some examples are shown in Fig. 1, for the W, Q^2, t variables, and the three helicity angles, θ_h, ϕ_h, and Φ_h, and in Fig. 2 for the transverse momentum p_T of the pions, for different Q^2 bins.

6 Systematics

The systematic uncertainties of the cross section were evaluated by varying the selection cuts and the MC simulation parameters. The following selection cuts were varied:

- the E - P_Z cut was changed within the appropriate resolution of ±3 GeV;
- the p_T of the pion tracks (default 0.15 GeV) was increased to 0.2 GeV;
- the distance of closest approach of the extrapolated track to the matched island in the CAL was changed from 30 cm to 20 cm;

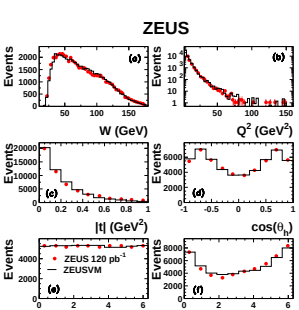

Figure 1
Comparison between the data and the ZEUSVM MC distributions for (*a*) W, (*b*) Q^2, (*c*) $|t|$, (*d*) $\cos\theta_h$, (*e*) ϕ_h and (*f*) Φ_h for events with $0.65 < M_{\pi\pi} < 1.1$ GeV and $|t| < 1.0$ GeV^2. The MC distributions are normalised to the data.

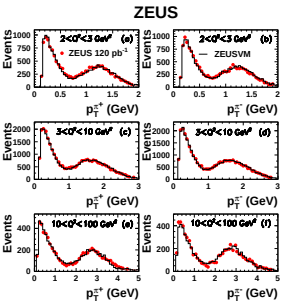

Figure 2
Comparison between the data and the ZEUSVM MC distributions for the transverse momentum, p_T, of π^+ and π^- particles, for different ranges of Q^2, as indicated in the figure. The events are selected to be within $0.65 < M_{\pi\pi} < 1.1$ GeV and $|t| < 1.0$ GeV^2. The MC distributions are normalised to the data.

- the $\pi^+\pi^-$-mass window was changed to 0.65–1.2 GeV;

- the Z vertex cut was varied by ±10 cm;

- the rectangular area of the electron impact point on the CAL was increased by 0.5 cm in X and Y ;

- the energy of an unmatched island was lowered to 0.25 GeV and then raised to 0.35 GeV.

The dependence of the results on the precision with which the MC reproduces the performance of the detector and the data was checked by varying the following inputs within their estimated uncertainty:

- the reconstructed position of the electron was shifted with respect to the MC by ±1 mm;

- the electron-position resolution was varied by ±10% in the MC;

- the W^δ-dependence in the MC was changed by varying δ by ±0.03;

- the exponential t-distribution in the MC was reweighted by changing the nominal slope parameter b by ±0.5 GeV^{-2};

- the angular distributions in the MC were reweighted assuming SCHC;

- the Q^2-distribution in the MC was reweighted by $(Q^2 + M_\rho^2)^k$, where $k = \pm 0.05$.

The largest uncertainty of about ±4% originated from the variation of the energy of the unmatched islands. All the other checks resulted on average in a 0.5% change in the measured cross sections. All the systematic uncertainties were added in quadrature. In addition, the cross-section measurements have an overall normalisation uncertainty of ±2% due to the luminosity measurement.

7 Proton dissociation

The production of ρ^0 mesons may be accompanied by the proton-dissociation process, $\gamma^* p \rightarrow \rho^0 N$. For low masses M_N of the dissociative system N, the hadronisation products may remain inside the beam-pipe, leaving no signals in the main detector. The contribution of these events to the exclusive ρ^0 cross section was estimated from MC generators for proton-dissociative processes.

A class of proton dissociative events for which the final-state particles leave observed signals in the surrounding detectors was used to tune the M_N and the t distribution in the MC. In the 1998–2000 running period, these events were selected by requiring a signal in the FPC detector with energy above 1 GeV. The comparison of the data with PYTHIA expectations for the energy distribution in the FPC is shown in Fig. 3(a). The same procedure was repeated with a sample of ρ^0 events for which the FPC energy was less than 1 GeV and a leading proton was measured in the LPS detector, with the fraction of the incoming proton momentum $x_L < 0.95$. The comparison between the x_L distribution measured in the data and that expected from PYTHIA is shown in Fig. 3(b), where the elastic peak in the data ($x_L > 0.95$) is also observed. Also shown in Fig. 3(c–e) is the fraction of proton-dissociative events expected in the selected ρ^0 sample as a function of Q^2, W and t. The fraction is at the level of 19%, independent of Q^2 and W, but increasing with increasing $|t|$. The combined use of the FPC and LPS methods leads to an estimate of the proton dissociative contribution for $|t| < 1$ GeV^2 of $0.19 \pm 0.02(\text{stat.}) \pm 0.03(\text{syst.})$. The systematic uncertainty was estimated by varying the parameters of the M_N distribution and by changing the FPC cut.

In the 1996–1997 data-taking period, a similar procedure was applied, after tuning the EPSOFT MC to reproduce events with hits in the PRT1 or energy deposits in the FCAL. The proton-dissociative contribution for $|t| < 1$ GeV^2 was determined to be 0.07 ± 0.02 after rejecting

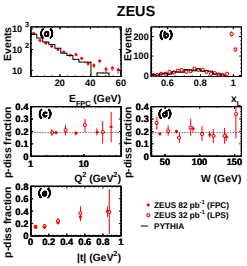

Figure 3

(*a*) The energy distribution in the FPC. The data (full dots) are compared to the expectations from the PYTHIA MC, normalised to the data. (*b*) The x_L distribution in the LPS. The data (open circles) are compared to the expectations from the PYTHIA MC, normalised to the data for $x_L < 0.95$. The extracted fraction of proton-dissociation events, from the FPC data (dots) and from the LPS data (open circles), as a function of (*c*) Q^2, (*d*) *W* and (*e*) |*t*|. All events were selected in the ρ^0 mass window (0.65–1.1 GeV). The dotted line in (*c*) and (*d*) represents a fit of a constant to the proton-dissociation fraction.

events with hits in the PRT1 or energy deposits in the FCAL. This number is consistent with that determined from the LPS and FPC because of the different angular coverage of the PRT1.

After subtraction of the proton-dissociative contribution, a good agreement between the cross sections derived from the two data-taking periods was found. For all the quoted cross sections integrated over *t*, the overall normalisation uncertainty due to the subtraction of the proton-dissociative contributions was estimated to be ± 4% and was not included in the systematic uncertainty. The proton-dissociative contribution was statistically subtracted in each analysed bin, unless stated otherwise.

8 Mass distributions

The $\pi^+\pi^-$-invariant-mass distribution is presented in Fig. 4. A clear enhancement in the ρ^0 region is observed. Background coming from the decay $\phi \to K^+K^-$, where the kaons are misidentified as pions, is expected [42] in the region $M_{\pi\pi} < 0.55$ GeV. That coming from ω events in the decay channel $\omega \to \pi^+\pi^-\pi^0$, where the π^0 remains undetected, contributes [42] in the region $M_{\pi\pi} < 0.65$ GeV. Therefore defining the selected ρ^0 events to be in the window $0.65 < M_{\pi\pi} < 1.1$ GeV ensures no background from these two channels.

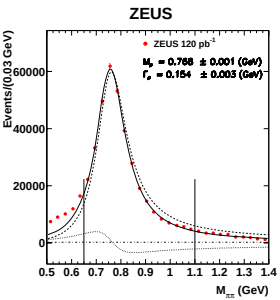

Figure 4
The $\pi^+\pi^-$ acceptance-corrected invariant-mass distribution. The line represent the best fit of the Söding form to the data in the range $0.65 < M_{\pi\pi} < 1.1$ GeV. The vertical lines indicate the range of masses used for the analysis. The dashed line is the shape of a relativistic Breit-Wigner with the fitted parameters given in the figure. The dotted line is the interference term between the non-resonant background (dash-dotted line) and the ρ^0 signal.

In order to estimate the non-resonant $\pi^+\pi^-$ background under the ρ^0, the Söding parameterisation [47] was fitted to the data, with results shown in the figure. The resulting mass and width values are in agreement with those given in the Particle Data Group [48] compilation. The integrated non-resonant background is of the order of 1% and is thus neglected.

The $\pi^+\pi^-$ mass distributions in different regions of Q^2 and t are shown in Fig. 5 and Fig. 6, respectively. The shape of the mass distribution changes neither with Q^2 nor with t. The results of the fit to the Söding parameterisation are also shown. Note that the interference term decreases with Q^2 as expected but is independent of t, indicating that the non-exclusive background is negligible.

9 Angular distributions and decay-matrix density

The exclusive electroproduction and decay of ρ^0 mesons is described, at fixed W, Q^2, $M_{\pi\pi}$ and t, by three helicity angles: Φ_h is the angle between the ρ^0 production plane and the electron scattering plane in the $\gamma^* p$ centre-of-mass frame; θ_h and ϕ_h are the polar and azimuthal angles of the positively charged decay pion in the s-channel helicity frame. In this frame, the spin-quantisation axis is defined as the direction opposite to the momentum of the final-state proton in the ρ^0 rest frame. In the $\gamma^* p$ centre-of-mass system, ϕ_h is the angle between the decay plane and the ρ^0 pro-

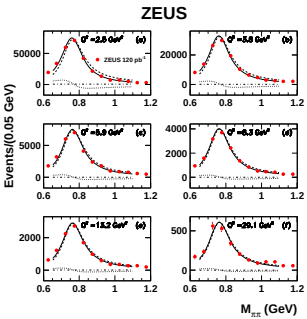

Figure 5
The $\pi^+\pi^-$ acceptance-corrected invariant-mass distribution, for different Q^2 intervals, with mean values as indicated in the figure. The lines are defined in the caption of Fig. 4.

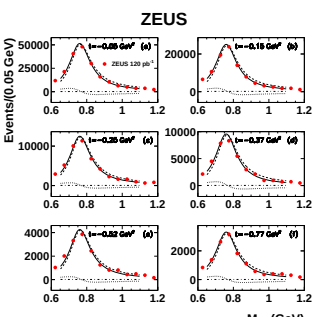

Figure 6
The $\pi^+\pi^-$ acceptance-corrected invariant-mass distribution, for different t intervals, with mean values as indicated in the figure. The lines are defined in the caption of Fig. 4.

duction plane. The angular distribution as a function of these three angles, $W(\cos\theta_h, \phi_h, \Phi_h)$, is parameterised by the ρ^0 spin-density matrix elements, ρ^α_{ik}, where $i, k = -1, 0, 1$ and by convention $\alpha = 0, 1, 2, 4, 5, 6$ for an unpolarised charged-lepton beam [49]. The superscript denotes the decomposition of the spin-density matrix into contributions from the following photon-polarisation states: unpolarised transverse photons (0); linearly polarised transverse photons (1,2); longitudinally polarised photons (4); and from the interference of the longitudinal and transverse amplitudes (5,6).

The decay angular distribution can be expressed in terms of combinations, r^{04}_{ik} and r^α_{ik}, of the density matrix elements

$$r^{04}_{ik} = \frac{\rho^0_{ik} + \varepsilon R \rho^4_{ik}}{1+\varepsilon R},$$

$$r^\alpha_{ik} = \begin{cases} \dfrac{\rho^\alpha_{ik}}{1+\varepsilon R}, & \alpha = 1,2 \\ \dfrac{\sqrt{R}\rho^\alpha_{ik}}{1+\varepsilon R}, & \alpha = 5,6, \end{cases}$$

where ε is the ratio of the longitudinal- to transverse-photon fluxes and $R = \sigma_L/\sigma_T$, with σ_L and σ_T the cross sections for exclusive ρ^0 production from longitudinal and transverse virtual photons, respectively. In the kinematic range of this analysis, the value of ε varies between 0.96 and 1 with an average value of 0.996; hence ρ^0_{ik} and ρ^4_{ik} cannot be distinguished.

The Hermitian nature of the spin-density matrix and the requirement of parity conservation reduces the number of independent parameters to 15 [49]. A 15-parameter fit was performed to the data and the obtained results are listed in Table 1 and shown in Fig. 7 as a function of Q^2. The published ZEUS results [50] at lower Q^2 values and the expectations of SCHC, when relevant, are also included. The observed Q^2 dependence, expected in some calculations [51] and previously reported by H1 [52], is driven by the R dependence on Q^2 under the assumption of helicity conservation and natural parity exchange. The significant deviation of r^5_{00} from zero shows that SCHC does not hold [51] as was observed previously [50,52].

The angular distribution for the decay of the ρ^0 meson, integrated over ϕ_h and Φ_h, reduces to

Table 1: Spin density matrix elements for electroproduction of ρ^0, for different intervals of Q^2. The first uncertainty is statistical, the second systematic.

Element	$2 < Q^2 < 3$ GeV^2	$3 < Q^2 < 4$ GeV^2	$4 < Q^2 < 6$ GeV^2	$6 < Q^2 < 10$ GeV^2	$10 < Q^2 < 100$ GeV^2
r^{04}_{00}	$0.590 \pm 0.006^{+0.012}_{-0.010}$	$0.659 \pm 0.008^{+0.009}_{-0.015}$	$0.725 \pm 0.008^{+0.014}_{-0.008}$	$0.752 \pm 0.008^{+0.011}_{-0.008}$	$0.814 \pm 0.010^{+0.008}_{-0.019}$
Re(r^{04}_{10})	$0.024 \pm 0.005^{+0.003}_{-0.009}$	$0.025 \pm 0.007^{+0.008}_{-0.009}$	$0.007 \pm 0.007^{+0.004}_{-0.017}$	$0.014 \pm 0.007^{+0.005}_{-0.010}$	$0.014 \pm 0.009^{+0.016}_{-0.007}$
r^{04}_{1-1}	$-0.009 \pm 0.007^{+0.008}_{-0.012}$	$-0.010 \pm 0.008^{+0.006}_{-0.016}$	$0.000 \pm 0.007^{+0.015}_{-0.006}$	$-0.016 \pm 0.007^{+0.018}_{-0.004}$	$-0.001 \pm 0.010^{+0.021}_{-0.006}$
r^{1}_{11}	$-0.008 \pm 0.007^{+0.006}_{-0.019}$	$-0.023 \pm 0.008^{+0.008}_{-0.016}$	$-0.015 \pm 0.008^{+0.010}_{-0.019}$	$-0.032 \pm 0.008^{+0.017}_{-0.001}$	$-0.002 \pm 0.011^{+0.008}_{-0.020}$
r^{1}_{00}	$-0.037 \pm 0.019^{+0.047}_{-0.014}$	$-0.014 \pm 0.026^{+0.046}_{-0.015}$	$0.020 \pm 0.028^{+0.072}_{-0.013}$	$0.019 \pm 0.030^{+0.008}_{-0.060}$	$-0.018 \pm 0.042^{+0.053}_{-0.034}$
Re(r^{1}_{10})	$-0.032 \pm 0.007^{+0.018}_{-0.004}$	$-0.023 \pm 0.010^{+0.008}_{-0.024}$	$-0.016 \pm 0.009^{+0.018}_{-0.013}$	$-0.006 \pm 0.011^{+0.003}_{-0.030}$	$-0.042 \pm 0.016^{+0.029}_{-0.009}$
r^{1}_{1-1}	$0.195 \pm 0.009^{+0.012}_{-0.019}$	$0.151 \pm 0.011^{+0.014}_{-0.011}$	$0.121 \pm 0.011^{+0.016}_{-0.011}$	$0.095 \pm 0.011^{+0.006}_{-0.029}$	$0.100 \pm 0.016^{+0.023}_{-0.032}$
Im(r^{2}_{10})	$0.040 \pm 0.007^{+0.010}_{-0.020}\pi$	$0.024 \pm 0.009^{+0.005}_{-0.020}$	$0.029 \pm 0.009^{+0.012}_{-0.011}$	$0.031 \pm 0.009^{+0.016}_{-0.012}$	$0.026 \pm 0.015^{+0.028}_{-0.005}$
Im(r^{2}_{1-1})	$-0.186 \pm 0.009^{+0.009}_{-0.024}$	$-0.148 \pm 0.011^{+0.019}_{-0.015}$	$-0.124 \pm 0.012^{+0.029}_{-0.013}$	$-0.107 \pm 0.011^{+0.004}_{-0.027}$	$-0.052 \pm 0.016^{+0.039}_{-0.012}$
r^{5}_{11}	$0.018 \pm 0.003^{+0.004}_{-0.005}$	$0.018 \pm 0.004^{+0.006}_{-0.004}$	$0.007 \pm 0.003^{+0.005}_{-0.007}$	$0.018 \pm 0.004^{+0.005}_{-0.002}$	$0.004 \pm 0.005^{+0.007}_{-0.003}$
r^{5}_{00}	$0.085 \pm 0.009^{+0.007}_{-0.015}$	$0.089 \pm 0.013^{+0.019}_{-0.016}$	$0.106 \pm 0.013^{+0.010}_{-0.016}$	$0.093 \pm 0.013^{+0.013}_{-0.010}$	$0.168 \pm 0.018^{+0.011}_{-0.020}$
Re(r^{5}_{10})	$0.167 \pm 0.003^{+0.007}_{-0.003}$	$0.164 \pm 0.004^{+0.005}_{-0.006}$	$0.143 \pm 0.005^{+0.004}_{-0.013}$	$0.132 \pm 0.005^{+0.004}_{-0.003}$	$0.110 \pm 0.007^{+0.011}_{-0.008}$
r^{5}_{1-1}	$0.000 \pm 0.005^{+0.006}_{-0.008}$	$-0.006 \pm 0.006^{+0.009}_{-0.006}$	$0.001 \pm 0.005^{+0.009}_{-0.003}$	$0.000 \pm 0.006^{+0.018}_{-0.003}$	$0.001 \pm 0.007^{+0.011}_{-0.002}$
Im(r^{6}_{10})	$-0.157 \pm 0.003^{+0.006}_{-0.004}$	$-0.147 \pm 0.004^{+0.004}_{-0.007}$	$-0.145 \pm 0.004^{+0.003}_{-0.009}$	$-0.135 \pm 0.004^{+0.007}_{-0.003}$	$-0.125 \pm 0.006^{+0.012}_{-0.002}$
Im(r^{6}_{1-1})	$0.010 \pm 0.005^{+0.004}_{-0.013}$	$-0.005 \pm 0.005^{+0.008}_{-0.005}$	$-0.001 \pm 0.005^{+0.005}_{-0.017}$	$0.008 \pm 0.005^{+0.003}_{-0.006}$	$-0.002 \pm 0.007^{+0.005}_{-0.007}$

$$W(\cos\theta_h) \propto \left[(1 - r^{04}_{00}) + (3r^{04}_{00} - 1)\cos^2\theta_h\right]. \quad (3)$$

The element r^{04}_{00} may be extracted from a one-dimensional fit to the $\cos\theta_h$ distribution. The $\cos\theta_h$ distributions, for different Q^2 intervals, are shown in Fig. 8, together with the results of a one-dimensional fit of the form (3). The data are well described by the fitted parameter r^{04}_{00} at each value of Q^2.

10 Cross section

The measured $\gamma^* p$ cross sections are averaged over intervals listed in the appropriate tables and are quoted at fixed values of Q^2 and W. The cross sections are corrected for the mass range $0.28 < M_{\pi\pi} < 1.5$ GeV and integrated over the full t-range, where applicable.

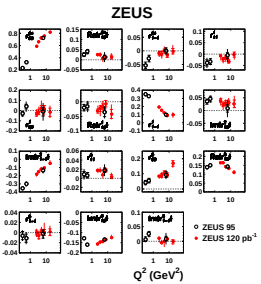

Figure 7
The 15 density-matrix elements obtained from a fit to the data (dots), as a function of Q^2. Also shown in the figure are results from an earlier measurement [50] (open circles). The inner error bars indicate the statistical uncertainty, the outer error bars represent the statistical and systematic uncertainty added in quadrature. The dotted line at zero is the expectation from SCHC when relevant.

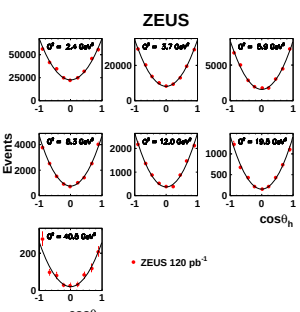

Figure 8
The acceptance-corrected cos θ_h distribution, for different Q^2 intervals, with mean values indicated in the figure. The line represent the fit to the data of Eq. (3).

10.1 t dependence of $\sigma(\gamma^* p \to \rho^0 p)$

The determination of $\sigma(\gamma^* p \to \rho^0 p)$ as a function of t for $W = 90$ GeV was performed by averaging over 40 $< W <$ 140 GeV. The differential cross-section $d\sigma/dt(\gamma^* p \to \rho^0 p)$ is shown in Fig. 9 and listed in Table 2, for different ranges of Q^2. An exponential form proportional to $e^{-b|t|}$ was fitted to the data in each range of Q^2; the results are shown in Fig. 10. The exponent b, listed in Table 3, decreases as a function of Q^2. After including the previous results at lower Q^2 [10,53], a sharp decrease of b is observed at low Q^2; the value of b then levels off at about 5 GeV^{-2}.

A compilation of the value of the slope b for exclusive VM electroproduction, as a function of $Q^2 + M^2$, is shown in Fig. 11. Here M is the mass of the corresponding final state. It also includes the exclusive production of a real photon, the deeply virtual Compton scattering (DVCS) measurement [54]. When b is plotted as a function of $Q^2 + M^2$, the trend of b decreasing with increasing scale to an asymptotic value of 5 GeV^{-2}, seems to be a universal property of exclusive processes, as expected in perturbative QCD [2].

10.2 Q^2 *dependence of* $\sigma(\gamma^* p \to \rho^0 p)$

The determination of $\sigma(\gamma^* p \to \rho^0 p)$ as a function of Q^2 for $W = 90$ GeV was performed by averaging over 40 $< W <$ 140 GeV. The results are shown in Fig. 12 with corresponding values given

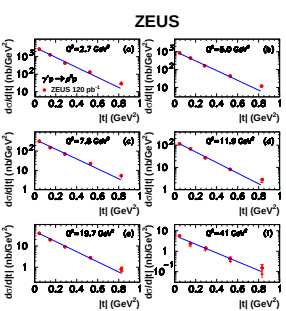

Figure 9
The differential cross-section $d\sigma/d|t|$ as a function of |t| for $\gamma^* p \to \rho^0 p$, for fixed values of Q^2, as indicated in the figure. The line represents an exponential fit to the data. The inner error bars indicate the statistical uncertainty, the outer error bars represent the statistical and systematic uncertainty added in quadrature.

Table 2: The differential cross-section $d\sigma/dt$ for the reaction $\gamma^* p \to \rho^0 p$ for different Q^2 intervals. The first column gives the Q^2 bin, while the second column gives the Q^2 value at which the cross section is quoted. The normalisation uncertainty due to luminosity (± 2%) and proton-dissociative background (± 4%), is not included.

Q^2 bin (GeV^2)	Q^2 (GeV^2)	$\lvert t \rvert$ (GeV^2)	$d\sigma/dt$ (nb/GeV^2)	stat.	syst.
2–4	2.7	0.05	2636.4	± 49.5	$^{+117.3}_{-155.3}$
2–4	2.7	0.15	1284.2	± 32.8	$^{+65.4}_{-87.7}$
2–4	2.7	0.29	450.7	± 13.5	$^{+30.8}_{-39.1}$
2–4	2.7	0.53	127.5	± 6.2	$^{+17.2}_{-17.0}$
2–4	2.7	0.83	28.1	± 3.3	$^{+10.3}_{-5.1}$
4–6.5	5.0	0.05	842.7	± 23.7	$^{+33.3}_{-40.5}$
4–6.5	5.0	0.15	415.8	± 15.4	$^{+18.9}_{-26.1}$
4–6.5	5.0	0.29	159.8	± 7.0	$^{+10.6}_{-13.8}$
4–6.5	5.0	0.53	43.7	± 3.2	$^{+5.7}_{-5.8}$
4–6.5	5.0	0.83	12.5	± 1.8	$^{+2.2}_{-2.2}$
6.5–10	7.8	0.05	338.4	± 10.8	$^{+15.4}_{-15.0}$
6.5–10	7.8	0.15	156.2	± 7.4	$^{+5.3}_{-13.3}$
6.5–10	7.8	0.29	67.3	± 3.3	$^{+4.9}_{-4.7}$
6.5–10	7.8	0.53	22.1	± 1.6	$^{+2.3}_{-3.1}$
6.5–10	7.8	0.83	5.03	± 0.94	$^{+1.48}_{-0.92}$
10–15	11.9	0.05	118.0	± 5.0	$^{+5.5}_{-5.7}$
10–15	11.9	0.15	70.2	± 3.9	$^{+5.2}_{-3.6}$
10–15	11.9	0.29	26.8	± 1.7	$^{+1.7}_{-2.6}$
10–15	11.9	0.53	8.40	± 0.76	$^{+0.97}_{-1.36}$
10–15	11.9	0.83	2.67	± 0.51	$^{+0.48}_{-0.52}$
15–30	19.7	0.05	39.6	± 2.2	$^{+1.7}_{-3.3}$

Table 2: The differential cross-section $d\sigma/dt$ for the reaction $\gamma^* p \to \rho^0 p$ for different Q^2 intervals. The first column gives the Q^2 bin, while the second column gives the Q^2 value at which the cross section is quoted. The normalisation uncertainty due to luminosity (± 2%) and proton-dissociative background (± 4%), is not included. *(Continued)*

15–30	19.7	0.15	20.4	± 1.5	$^{+1.9}_{-1.4}$
15–30	19.7	0.29	9.12	± 0.71	$^{+0.59}_{-0.94}$
15–30	19.7	0.53	2.73	± 0.31	$^{+0.39}_{-0.38}$
15–30	19.7	0.83	0.84	± 0.19	$^{+0.19}_{-0.30}$
30–80	41.0	0.05	5.44	± 0.83	$^{+0.76}_{-0.80}$
30–80	41.0	0.15	2.28	± 0.50	$^{+0.37}_{-0.54}$
30–80	41.0	0.29	1.40	± 0.26	$^{+0.26}_{-0.35}$
30–80	41.0	0.53	0.42	± 0.11	$^{+0.07}_{-0.11}$
30–80	41.0	0.83	0.15	± 0.07	$^{+0.06}_{-0.07}$

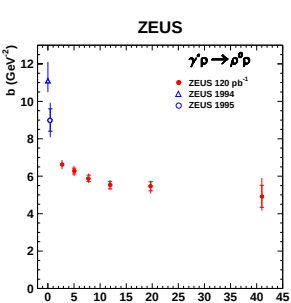

Figure 10
The value of the slope b from a fit of the form $d\sigma/d|t| \propto e^{-b|t|}$ for exclusive ρ^0 electroproduction, as a function of Q^2. Also shown are values of b obtained previously at lower Q^2 values [10, 53]. The inner error bars indicate the statistical uncertainty, the outer error bars represent the statistical and systematic uncertainty added in quadrature.

Table 3: The slope *b* resulting from a fit to the differential cross-section $d\sigma/dt$ to an exponential form for the reaction $\gamma^* p \to \rho^0 p$, for different Q^2 intervals. The first column gives the Q^2 bin, while the second column gives the Q^2 value at which the differential cross sections are quoted. The first uncertainty is statistical, the second systematic.

Q^2 bin (GeV^2)	Q^2 (GeV^2)	b (GeV^{-2})
2–4	2.7	$6.6 \pm 0.1^{+0.2}_{-0.2}$
4–6.5	5.0	$6.3 \pm 0.2^{+0.2}_{-0.2}$
6.5–10	7.8	$5.9 \pm 0.2^{+0.2}_{-0.2}$
10–15	11.9	$5.5 \pm 0.2^{+0.3}_{-0.2}$
15–30	19.7	$5.5 \pm 0.3^{+0.3}_{-0.3}$
30–80	41.0	$4.9 \pm 0.6^{+0.8}_{-0.5}$

in Table 4. As expected, a steep decrease of the cross section with Q^2 is observed. The photoproduction and the low-Q^2 (< 1 GeV^2) measurements are also shown in the figure. An attempt to fit the Q^2 dependence with a simple propagator term

$$\sigma(\gamma^* p \to \rho^0 p) \sim (Q^2 + m_\rho^2)^{-n},$$

with the normalisation and n as free parameters, failed to produce results with an acceptable χ^2. The data appear to favour an n value which increases with Q^2.

10.3 W dependence of $\sigma(\gamma^* p \to \rho^0 p)$

The values of the cross section $\sigma(\gamma^* p \to \rho^0 p)$ as a function of W, for fixed values of Q^2, are plotted in Fig. 13 and given in Table 5. The cross sections increase with increasing W, with the rate of increase growing with increasing Q^2.

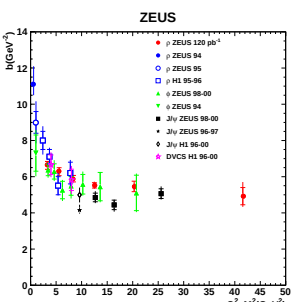

Figure 11
A compilation of the value of the slope b from a fit of the form $d\sigma/d|t| \propto e^{-b|t|}$ for exclusive vector-meson electroproduction, as a function of $Q^2 + M^2$. Also included is the DVCS result. The inner error bars indicate the statistical uncertainty, the outer error bars represent the statistical and systematic uncertainty added in quadrature.

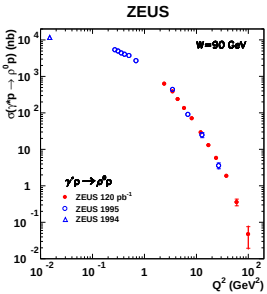

Figure 12
The Q^2 dependence of the cross section for exclusive ρ^0 electroproduction, at a $\gamma^* p$ centre-of-mass energy $W = 90$ GeV. The ZEUS 1994 [53] and the ZEUS 1995 [10] data points have been extrapolated to $W = 90$ GeV using the parameterisations reported in the respective publications. The inner error bars indicate the statistical uncertainty, the outer error bars represent the statistical and systematic uncertainty added in quadrature.

Table 4: Cross-section measurements at Q^2 and $W = 90$ GeV averaged over the Q^2 and W intervals given in the table. The normalisation uncertainty due to luminosity (± 2%) and proton-dissociative background (± 4%) is not included.

Q^2 bin (GeV^2)	W bin (GeV)	Q^2 (GeV^2)	W (GeV)	$\sigma(\gamma^* p \to \rho^0 p)$ (nb)	stat.	syst.
2–3	40–100	2.4	90	647.1	± 8.7	$^{+28.4}_{-41.7}$
3–4	40–100	3.4	90	396.7	± 6.7	$^{+14.6}_{-19.4}$
4–5	40–100	4.4	90	247.8	± 5.8	$^{+8.9}_{-12.6}$
5–7	40–120	5.8	90	140.3	± 2.6	$^{+3.9}_{-5.9}$
7–10	40–140	8.2	90	71.9	± 1.4	$^{+1.7}_{-2.8}$
10–15	40–140	12	90	29.73	± 0.68	$^{+0.75}_{-1.14}$
15–20	40–140	17	90	12.77	± 0.50	$^{+0.27}_{-0.42}$
20–30	40–140	24	90	6.03	± 0.31	$^{+0.37}_{-0.13}$
30–50	40–140	37	90	1.88	± 0.16	$^{+0.07}_{-0.15}$
50–80	40–140	60	90	0.36	± 0.07	$^{+0.04}_{-0.03}$
80–160	40–140	100	90	0.05	± 0.03	$^{+0.02}_{-0.01}$

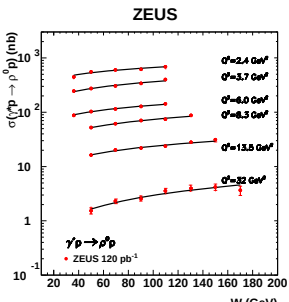

Figure 13
The W dependence of the cross section for exclusive ρ^0 electroproduction, for different Q^2 values, as indicated in the figure. The inner error bars indicate the statistical uncertainty, the outer error bars represent the statistical and systematic uncertainty added in quadrature. The lines are the result of a fit of the form W^δ to the data.

In order to quantify the rate of growth and its significance, the W dependence for each Q^2 value was fitted to the functional form

$$\sigma \sim W^\delta.$$

The resulting δ values are presented as a function of Q^2 in Fig. 14 and listed in Table 6. For completeness, the δ values from lower Q^2 are also included. A clear increase of δ with Q^2 is observed. Such an increase is expected in pQCD, and reflects the change of the low-x gluon distribution of the proton with Q^2.

To facilitate the comparison, the ZEUS cross-section data as a function of W have been replotted in the Q^2 bins used by H1 [9]. The results are shown in Fig. 15. The agreement between the two measurements is reasonable. However, in some Q^2 bins the shape of the W dependence is somewhat different.

A compilation of the value of the slope δ for exclusive VM electroproduction, as a function of $Q^2 + M^2$, is shown in Fig. 16. It also includes the DVCS result [54]. When plotted as a function of $Q^2 + M^2$, the value of δ and its increase with the scale are similar for all the exclusive processes, as expected in perturbative QCD [2].

Table 5: Cross-sections values obtained at Q^2 and *W* as a result of averaging over bins of the Q^2 and *W* intervals given in the table. The normalisation uncertainty due to luminosity (± 2%) and proton-dissociative background (± 4%), are not included.

Q^2 bin (GeV^2)	*W* bin (GeV)	Q^2 (GeV^2)	W (GeV)	$\sigma(\gamma^* p \rightarrow \rho^0 p)$ (nb)	stat.	syst.
2–3	32–40	2.4	36.0	451.9	± 15.1	$^{+25.2}_{-43.6}$
2–3	40–60	2.4	50.0	554.1	± 11.5	$^{+31.6}_{-39.2}$
2–3	60–80	2.4	70.0	599.9	± 13.9	$^{+28.5}_{-38.5}$
2–3	80–100	2.4	90.0	622.5	± 17.3	$^{+33.8}_{-43.2}$
2–3	100–120	2.4	110.0	690.1	± 30.3	$^{+40.8}_{-66.9}$
3–5	32–40	3.7	36.0	240.8	± 8.0	$^{+9.5}_{-15.5}$
3–5	40–60	3.7	50.0	277.5	± 5.9	$^{+12.2}_{-15.3}$
3–5	60–80	3.7	70.0	303.7	± 7.3	$^{+11.1}_{-14.4}$
3–5	80–100	3.7	90.0	344.6	± 9.4	$^{+10.4}_{-17.2}$
3–5	100–120	3.7	110.0	404.7	± 15.5	$^{+15.2}_{-22.5}$
5–7	32–40	6.0	36.0	88.5	± 5.1	$^{+6.0}_{-4.1}$
5–7	40–60	6.0	50.0	104.9	± 3.6	$^{+3.6}_{-6.9}$
5–7	60–80	6.0	70.0	113.6	± 4.1	$^{+6.0}_{-3.9}$
5–7	80–100	6.0	90.0	127.6	± 4.9	$^{+4.0}_{-5.8}$
5–7	100–120	6.0	110.0	144.0	± 6.1	$^{+8.6}_{-8.4}$
7–10	40–60	8.3	50.0	52.3	± 1.9	$^{+1.7}_{-2.7}$
7–10	60–80	8.3	70.0	61.7	± 2.4	$^{+2.1}_{-2.9}$
7–10	80–100	8.3	90.0	70.1	± 2.9	$^{+2.0}_{-3.3}$
7–10	100–120	8.3	110.0	75.2	± 3.4	$^{+3.1}_{-3.0}$
7–10	120–140	8.3	130.0	87.5	± 4.7	$^{+2.5}_{-4.1}$
10–22	40–60	13.5	50.0	16.4	± 0.6	$^{+0.6}_{-0.7}$
10–22	60–80	13.5	70.0	20.2	± 0.8	$^{+0.8}_{-0.7}$

Table 5: Cross-sections values obtained at Q^2 and W as a result of averaging over bins of the Q^2 and W intervals given in the table. The normalisation uncertainty due to luminosity (± 2%) and proton-dissociative background (± 4%), are not included. *(Continued)*

10–22	80–100	13.5	90.0	21.9	± 0.9	$^{+0.7}_{-0.9}$
10–22	100–120	13.5	110.0	24.3	± 1.1	$^{+0.9}_{-1.2}$
10–22	120–140	13.5	130.0	27.7	± 1.4	$^{+0.9}_{-1.0}$
10–22	140–160	13.5	150.0	30.7	± 2.3	$^{+1.2}_{-1.1}$
22–80	40–60	32.0	50.0	1.5	± 0.2	$^{+0.2}_{-0.1}$
22–80	60–80	32.0	70.0	2.3	± 0.2	$^{+0.1}_{-0.1}$
22–80	80–100	32.0	90.0	2.6	± 0.3	$^{+0.3}_{-0.2}$
22–80	100–120	32.0	110.0	3.6	± 0.4	$^{+0.1}_{-0.3}$
22–80	120–140	32.0	130.0	4.0	± 0.5	$^{+0.2}_{-0.4}$
22–80	140–160	32.0	150.0	4.2	± 0.6	$^{+0.2}_{-0.4}$
22–80	160–180	32.0	170.0	3.6	± 0.7	$^{+0.3}_{-0.3}$

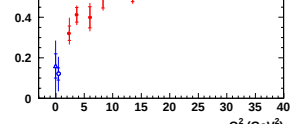

Figure 14
The value of δ from a fit of the form W^{δ} for exclusive ρ^0 electroproduction, as a function of Q^2. Also shown are values of δ obtained previously at lower Q^2 values [10, 53]. The inner error bars indicate the statistical uncertainty, the outer error bars represent the statistical and systematic uncertainty added in quadrature.

Table 6: The value of δ obtained from fitting $\sigma^{\gamma^* p \to \rho^0 p} \propto W^{\delta}$. The first column gives the Q^2 bin, while the second column gives the Q^2 value at which the cross section was quoted.

Q^2 bin (GeV^2)	Q^2 (GeV^2)	δ	stat.	syst.
2–3	2.4	0.321	± 0.035	+0.068 −0.043
3–5	3.7	0.412	± 0.036	+0.029 −0.035
5–7	6.0	0.400	± 0.052	+0.048 −0.045
7–10	8.3	0.503	± 0.057	+0.047 −0.041
10–22	13.5	0.529	± 0.051	+0.030 −0.035
22–80	32.0	0.834	± 0.118	+0.043 −0.112

I I $R = \sigma_L/\sigma_T$ and r_{00}^{04}

The SCHC hypothesis implies that $r_{1-1}^1 = -\mathrm{Im}\{r_{1-1}^2\}$ and $\mathrm{Re}\{r_{10}^5\} = -\mathrm{Im}\{r_{10}^6\}$. In this case, the ratio $R = \sigma_L/\sigma_T$ can be related to the r_{00}^{04} matrix element,

$$R = \frac{1}{\varepsilon}\frac{r_{00}^{04}}{1-r_{00}^{04}}, \qquad (4)$$

and thus can be extracted from the θ_n distribution alone.

If the SCHC requirement is relaxed, then the relation between R and r_{00}^{04} is modified,

$$R = \frac{1}{\varepsilon}\frac{r_{00}^{04}-\Delta^2}{1-(r_{00}^{04}-\Delta^2)},$$

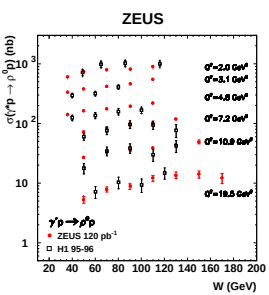

Figure 15

Comparison of the H1 (squares) and ZEUS (dots) measurements of the W dependence of $\sigma^{\gamma^* p \to \rho^0 p}$, for different Q^2 values, as indicated in the figure. The inner error bars indicate the statistical uncertainty, the outer error bars represent the statistical and systematic uncertainty added in quadrature.

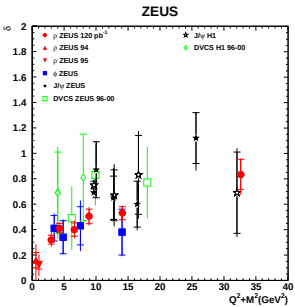

Figure 16
A compilation of the value of δ from a fit of the form W^{δ} for exclusive vector-meson electroproduction, as a function of $Q^2 + M^2$. It includes also the DVCS results. The inner error bars indicate the statistical uncertainty, the outer error bars represent the statistical and systematic uncertainty added in quadrature.

with

$$\Delta \simeq \frac{r_{00}^{5}}{\sqrt{2r_{00}^{04}}}.$$

In the kinematic range of the measurements presented in this paper, the non-zero value of Δ implies a correction of ~3% on R up to the highest Q^2 value, where it is ~10%, and is neglected.

Under the assumption that Eq. (4) is valid and for values of ε studied in this paper, $<\varepsilon> = 0.996$, the matrix element r_{00}^{04} may be interpreted as

$$r_{00}^{04} = \sigma_L/\sigma_{tot},$$

where $\sigma_{tot} = \sigma_L + \sigma_T$. When the value of r_{00}^{04} is close to one, as is the case for this analysis, the error on R becomes large and highly asymmetrical. It is then advantageous to study the properties of r_{00}^{04} itself which carries the same information, rather than R.

The Q^2 dependence of r_{00}^{04} for W = 90 GeV, averaged over the range 40 <W < 140 GeV, is shown in Fig. 17 and listed in Table 7 together with the corresponding R values. The figure includes three data points at lower Q^2 from previous studies [10,53]. An initial steep rise of r_{00}^{04} with Q^2 is observed and above $Q^2 \simeq 10$ GeV^2, the rise with Q^2 becomes milder. At Q^2 = 40 GeV^2, σ_L constitutes about 90% of the total $\gamma^* p$ cross section.

The comparison of the H1 and ZEUS results is presented in Fig. 18 in terms of the ratio R. The H1 measurements are at W = 75 GeV and those of ZEUS at W = 90 GeV. Given the fact that R seems to be independent of W (see below), both data sets can be directly compared. The two measurements are in good agreement.

The dependence of R on $M_{\pi\pi}$ is presented in Fig. 19 for two Q^2 intervals. The value of R falls rapidly with $M_{\pi\pi}$ above the central ρ^0 mass value. Although a change of R with $M_{\pi\pi}$ was anticipated to be ~10% [55], the effect seen in the data is much stronger. The effect remains strong also at higher Q^2, contrary to expectations [55]. Once averaged over the ρ^0 mass region, the main contribution to R comes from the central ρ^0 mass value.

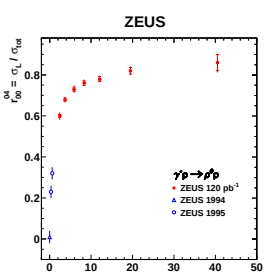

Figure 17

The ratio r_{00}^{04} as a function of Q^2 for W = 90 GeV. Also included are values of r_{00}^{04} from previous measurements at lower Q^2 values [10, 53]. The inner error bars indicate the statistical uncertainty, the outer error bars represent the statistical and systematic uncertainty added in quadrature.

Table 7: The spin matrix element r_{00}^{04} and the ratio of cross sections for longitudinally and transversely polarised photons, $R = \sigma_L/\sigma_T$, as a function of Q^2, averaged over the Q^2 and W bins given in the table. The first uncertainty is statistical, the second systematic.

Q^2 bin (GeV^2)	Q^2 (GeV^2)	W bin (GeV)	r_{00}^{04}	$R = \sigma_L/\sigma_T$
2–3	2.4	32–120	$0.60 \pm 0.01^{+0.03}_{-0.03}$	$1.50^{+0.05}_{-0.05}{}^{+0.20}_{-0.15}$
3–5	3.7	32–120	$0.68 \pm 0.01^{+0.02}_{-0.02}$	$2.10^{+0.08}_{-0.08}{}^{+0.18}_{-0.14}$
5–7	5.9	40–140	$0.73 \pm 0.01^{+0.01}_{-0.02}$	$2.70^{+0.14}_{-0.13}{}^{+0.26}_{-0.28}$
7–10	8.3	40–140	$0.76 \pm 0.01^{+0.01}_{-0.02}$	$3.20^{+0.20}_{-0.18}{}^{+0.25}_{-0.27}$
10–15	12.0	40–140	$0.78 \pm 0.01^{+0.01}_{-0.01}$	$3.50^{+0.26}_{-0.24}{}^{+0.30}_{-0.26}$
15–30	19.5	40–140	$0.82 \pm 0.02^{+0.01}_{-0.02}$	$4.60^{+0.54}_{-0.45}{}^{+0.48}_{-0.44}$
30–100	40.5	40–160	$0.86 \pm 0.04^{+0.03}_{-0.02}$	$6.10^{+2.75}_{-1.56}{}^{+2.15}_{-0.85}$

The W dependence of r_{00}^{04}, for different values of Q^2, is shown in Fig. 20 and listed in Table 8. Within the measurement uncertainties, r_{00}^{04} is independent of W, for all Q^2 values. This implies that the W behaviour of σ_L is the same as that of σ_T, a result which is somewhat surprising. The

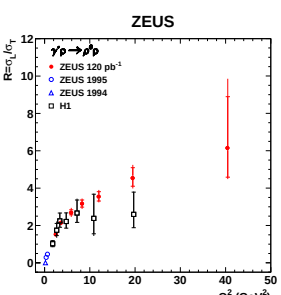

Figure 18
Comparison of the H1 (squares) and ZEUS (dots) measurements of R as a function of Q^2. The H1 data are at W = 75 GeV and those of ZEUS at W = 90 GeV. Also included are measurements performed previously at lower Q^2 values [10, 53]. The inner error bars indicate the statistical uncertainty, the outer error bars represent the statistical and systematic uncertainty added in quadrature.

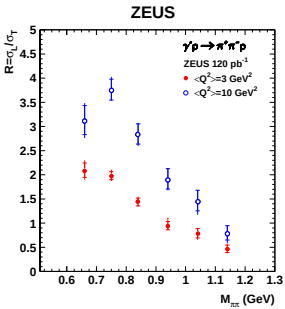

Figure 19
The ratio R as a function of $M_{\pi\pi}$, for W = 80 GeV, and for two values of Q^2, as indicated in the figure. The inner error bars indicate the statistical uncertainty, the outer error bars represent the statistical and systematic uncertainty added in quadrature.

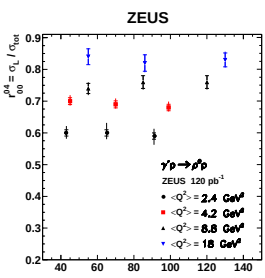

Figure 20
The ratio r_{00}^{04}, as a function of W for different values of Q^2, as indicated in the figure. The inner error bars indicate the statistical uncertainty, the outer error bars represent the statistical and systematic uncertainty added in quadrature.

Table 8: The spin matrix element r_{00}^{04} and the ratio of cross sections for longitudinally and transversely polarised photons, $R = \sigma_L/\sigma_T$, as a function of *W* for different values of Q^2, averaged over the Q^2 and *W* bins given in the table. The first uncertainty is statistical, the second systematic.

Q^2 bin (GeV^2)	Q^2 (GeV^2)	*W* bin (GeV)	*W* (GeV)	r_{00}^{04}	$R = \sigma_L/\sigma_T$
2–3	2.4	32–55	43	$0.60 \pm 0.01^{+0.03}_{-0.02}$	$1.50^{+0.06}_{-0.06}{}^{+0.21}_{-0.15}$
2–3	2.4	55–75	65	$0.60 \pm 0.01^{+0.05}_{-0.03}$	$1.50^{+0.06}_{-0.06}{}^{+0.35}_{-0.17}$
2–3	2.4	75–110	91	$0.59 \pm 0.01^{+0.04}_{-0.04}$	$1.43^{+0.06}_{-0.06}{}^{+0.23}_{-0.23}$
3–7	4.2	32–60	45	$0.70 \pm 0.01^{+0.01}_{-0.01}$	$2.33^{+0.09}_{-0.09}{}^{+0.13}_{-0.09}$
3–7	4.2	60–80	70	$0.69 \pm 0.01^{+0.02}_{-0.01}$	$2.23^{+0.12}_{-0.11}{}^{+0.24}_{-0.10}$
3–7	4.2	80–120	99	$0.69 \pm 0.01^{+0.01}_{-0.01}$	$2.23^{+0.10}_{-0.09}{}^{+0.14}_{-0.09}$
7–12	8.8	40–70	55	$0.74 \pm 0.01^{+0.01}_{-0.02}$	$2.85^{+0.25}_{-0.22}{}^{+0.23}_{-0.26}$
7–12	8.8	70–100	85	$0.76 \pm 0.02^{+0.01}_{-0.02}$	$3.17^{+0.38}_{-0.32}{}^{+0.19}_{-0.28}$
7–12	8.8	100–140	120	$0.76 \pm 0.02^{+0.01}_{-0.02}$	$3.17^{+0.38}_{-0.32}{}^{+0.23}_{-0.26}$
12–50	18.0	40–70	55	$0.84 \pm 0.03^{+0.01}_{-0.01}$	$5.25^{+1.16}_{-0.84}{}^{+0.54}_{-0.34}$
12–50	18.0	70–100	85	$0.82 \pm 0.03^{+0.01}_{-0.02}$	$4.55^{+0.94}_{-0.70}{}^{+0.47}_{-0.43}$
12–50	18.0	100–160	130	$0.83 \pm 0.02^{+0.02}_{-0.01}$	$4.88^{+0.87}_{-0.67}{}^{+0.64}_{-0.39}$

$q\bar{q}$ configurations in the wave function of γ_L^* have typically a small transverse size, while the configurations contributing to γ_T^* may have large transverse size. The contribution to σ_T of large-size $q\bar{q}$ configurations, which are more hadron-like, is expected to lead to a shallower *W* dependence than in case of σ_L. Thus, the result presented in Fig. 20 suggests that the large-size configurations of the transversely polarised photon are suppressed.

The above conclusion can also explain the behaviour of r_{00}^{04} as a function of *t*, shown in Fig. 21 and presented in Table 9 for two Q^2 values. Different sizes of interacting objects imply different *t* distributions, in particular a steeper $d\sigma_T/dt$ compared to $d\sigma_L/dt$. This turns out not to be the case. In both Q^2 ranges, r_{00}^{04} is independent of *t*, reinforcing the earlier conclusion about the suppression of the large-size configurations in the transversely polarised photon.

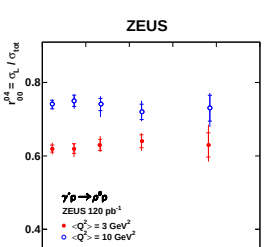

Figure 21

The ratio r^{04}_{00} as a function of |t| for different values of Q^2, as indicated in the figure. The inner error bars indicate the statistical uncertainty, the outer error bars represent the statistical and systematic uncertainty added in quadrature.

Table 9: The spin matrix element r^{04}_{00} and the ratio of cross sections for longitudinally and transversely polarised photons, $R = \sigma_L/\sigma_T$, as a function of |t| for two values of Q^2, averaged over the Q^2 and *W* bins given in the table. The first uncertainty is statistical, the second systematic.

Q^2 bin (GeV^2)	Q^2 (GeV^2)	*W* bin (GeV)	|t| (GeV^2)	r^{04}_{00}	$R = \sigma_L/\sigma_T$
2–5	3.0	32–120	0.04	$0.62 \pm 0.01^{+0.02}_{-0.02}$	$1.63^{+0.07}_{-0.06}{}^{+0.15}_{-0.13}$
2–5	3.0	32–120	0.14	$0.62 \pm 0.01^{+0.01}_{-0.03}$	$1.63^{+0.09}_{-0.09}{}^{+0.10}_{-0.19}$
2–5	3.0	32–120	0.27	$0.63 \pm 0.01^{+0.04}_{-0.02}$	$1.70^{+0.11}_{-0.11}{}^{+0.24}_{-0.14}$
2–5	3.0	32–120	0.45	$0.64 \pm 0.02^{+0.02}_{-0.03}$	$1.78^{+0.14}_{-0.13}{}^{+0.16}_{-0.21}$
2–5	3.0	32–120	0.76	$0.63 \pm 0.03^{+0.07}_{-0.05}$	$1.70^{+0.26}_{-0.22}{}^{+0.63}_{-0.32}$
5–50	10.0	40–160	0.04	$0.74 \pm 0.01^{+0.01}_{-0.01}$	$2.84^{+0.18}_{-0.17}{}^{+0.16}_{-0.15}$
5–50	10.0	40–160	0.15	$0.75 \pm 0.01^{+0.01}_{-0.02}$	$3.00^{+0.26}_{-0.23}{}^{+0.17}_{-0.30}$
5–50	10.0	40–160	0.27	$0.74 \pm 0.02^{+0.02}_{-0.04}$	$2.84^{+0.26}_{-0.24}{}^{+0.32}_{-0.51}$
5–50	10.0	40–160	0.45	$0.72 \pm 0.02^{+0.03}_{-0.02}$	$2.57^{+0.29}_{-0.25}{}^{+0.41}_{-0.22}$
5–50	10.0	40–160	0.76	$0.73 \pm 0.04^{+0.03}_{-0.05}$	$2.70^{+0.56}_{-0.43}{}^{+0.45}_{-0.57}$

12 Effective Pomeron trajectory

An effective Pomeron trajectory can be determined from exclusive ρ^0 electroproduction by using Eq. (2). Since the W dependence of the proton-dissociative contribution was established to be the same as the exclusive ρ^0 sample, no subtraction for proton-dissociative events was performed.

A study of the W dependence of the differential $d\sigma/dt$ cross section at fixed t results in values of $\alpha_{\mathbb{P}}(t)$, listed in Table 10 and displayed in Fig. 22, for $Q^2 = 3$ GeV^2 (upper plot) and 10 GeV^2 (lower plot). A linear fit of the form of Eq. (1), shown in the figures, yields values of $\alpha_{\mathbb{P}}(0)$ and $\alpha'_{\mathbb{P}}$ shown in Fig. 23, and listed in Table 11. The value of $\alpha_{\mathbb{P}}(0)$ increases slightly with Q^2, while the value of $\alpha'_{\mathbb{P}}$ is Q^2 independent, within the measurement uncertainties. Its value tends to be lower than that of the soft Pomeron [56].

An alternative way of measuring the slope of the Pomeron trajectory is to study the W dependence of the b slope, for fixed Q^2 values. Figure 24 displays the values of b as a function of W for two Q^2 intervals (see also Table 12). The curves are a result of fitting the data to the expression $b = b_0 + 4\alpha'_{\mathbb{P}} \ln(W/W_0)$. The resulting slopes of the trajectory are $\alpha'_{\mathbb{P}} = 0.15 \pm 0.04\ (stat.)^{+0.04}_{-0.06}\ (syst.)$ for $<Q^2> = 3.5$ GeV^2 and $\alpha'_{\mathbb{P}} = 0.04 \pm 0.06\ (stat.)^{+0.07}_{-0.02}\ (syst.)$ for $<Q^2> = 11$ GeV^2. These results are consistent with those presented in Table 11.

13 Comparison to models

In this section, predictions from several pQCD-inspired models are compared to the measurements.

Table 10: The values of the effective Pomeron trajectory $\alpha_{\mathbb{P}}(t)$ as a function of |t|, for two Q^2 values. The first uncertainty is statistical, the second systematic.

Q^2 bin (GeV^2)	Q^2 (GeV^2)	|t| (GeV^2)	$\alpha_{\mathbb{P}}(t)$
2–5	3	0.04	$1.104 \pm 0.011^{+0.010}_{-0.010}$
2–5	3	0.14	$1.099 \pm 0.014^{+0.011}_{-0.025}$
2–5	3	0.28	$1.048 \pm 0.016^{+0.038}_{-0.014}$
2–5	3	0.57	$1.013 \pm 0.021^{+0.041}_{-0.017}$
5–50	10	0.04	$1.149 \pm 0.012^{+0.015}_{-0.006}$
5–50	10	0.16	$1.134 \pm 0.014^{+0.005}_{-0.027}$
5–50	10	0.35	$1.104 \pm 0.017^{+0.012}_{-0.011}$
5–50	10	0.68	$1.085 \pm 0.028^{+0.042}_{-0.031}$

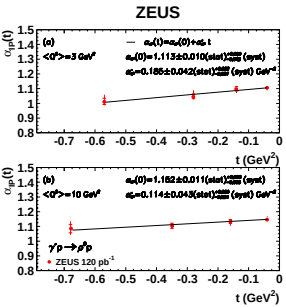

Figure 22

The effective Pomeron trajectory $\alpha_{\mathbb{P}}(t)$ as a function of t, for two values of Q^2, with average values indicated in the figure. The inner error bars indicate the statistical uncertainty, the outer error bars represent the statistical and systematic uncertainty added in quadrature.

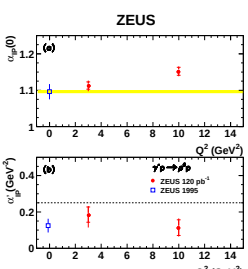

Figure 23

The parameters of the effective Pomeron trajectory in exclusive ρ^0 electroproduction, (*a*) $\alpha_{\mathbb{P}}(0)$ and (*b*) $\alpha'_{\mathbb{P}}$, as a function of Q^2. The inner error bars indicate the statistical uncertainty, the outer error bars represent the statistical and systematic uncertainty added in quadrature. The band in (*a*) and the dashed line in (*b*) are at the values of the parameters of the soft Pomeron [19, 20].

Table 11: The values of the effective Pomeron trajectory intercept $\alpha_{\mathbb{P}}(0)$ and slope $\alpha'_{\mathbb{P}}$, for two Q^2 values. The first uncertainty is statistical, the second systematic.

Q^2 bin (GeV^2)	Q^2(GeV^2)	$\alpha_{\mathbb{P}}(0)$	$\alpha'_{\mathbb{P}}$ (GeV^{-2})
2–5	3	$1.113 \pm 0.010^{+0.009}_{-0.012}$	$0.185 \pm 0.042^{+0.022}_{-0.057}$
5–50	10	$1.152 \pm 0.011^{+0.006}_{-0.006}$	$0.114 \pm 0.043^{+0.026}_{-0.024}$

13.1 The models

All models are based on the dipole representation of the virtual photon, in which the photon first fluctuates into a $q\bar{q}$ pair (the colour dipole), which then interacts with the proton to produce the ρ^0. The ingredients necessary in such calculations are the virtual-photon wave-function, the dipole-proton cross section, and the ρ^0 wave-function. The photon wave-function is known from QED. The models differ in the treatment of the dipole-proton cross section and the assumed ρ^0 wave-function.

The models of Frankfurt, Koepf and Strikman (FKS) [57,58] and of Martin, Ryskin and Teubner (MRT) [59,60] are based on two-gluon exchange as the dominant mechanism for the dipole-proton interaction. The gluon distributions are derived from inclusive measurements of the pro-

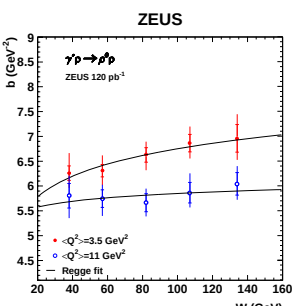

Figure 24
The b slope as a function of W for two ranges of Q^2, with average values as indicated in the figure. The inner error bars indicate the statistical uncertainty, the outer error bars represent the statistical and systematic uncertainty added in quadrature. The lines are the results of fitting Eq. (2) to the data.

Table 12: The slope b resulting from a fit of the differential cross section $d\sigma/dt$ for the reaction $\gamma^* p \to \rho^0 p$ to an exponential form, for different W values, for two Q^2 values. The first uncertainty is statistical, the second systematic.

Q^2 (GeV^2)	W (GeV)	b (GeV^{-2})
3.5	38	$6.3 \pm 0.2^{+0.4}_{-0.3}$
3.5	57	$6.3 \pm 0.1^{+0.3}_{-0.3}$
3.5	82	$6.6 \pm 0.2^{+0.2}_{-0.3}$
3.5	107	$6.9 \pm 0.2^{+0.3}_{-0.3}$
3.5	134	$7.0 \pm 0.3^{+0.4}_{-0.3}$
11	38	$5.8 \pm 0.3^{+0.3}_{-0.4}$
11	57	$5.8 \pm 0.2^{+0.2}_{-0.3}$
11	82	$5.7 \pm 0.2^{+0.2}_{-0.2}$
11	107	$5.9 \pm 0.2^{+0.3}_{-0.2}$
11	134	$6.1 \pm 0.2^{+0.3}_{-0.2}$

ton structure function. In the FKS model, a three-dimensional Gaussian is assumed for the ρ^0 wave-function, while MRT use parton-hadron duality and normalise the calculations to the data. For the comparison with the present measurements the MRST99 [61] and CTEQ6.5M [62] parameterisations for the gluon density were used.

Kowalski, Motyka and Watt (KMW) [63] use an improved version of the saturation model [64,65], with an explicit dependence on the impact parameter and DGLAP [66-69] evolution in Q^2, introduced through the unintegrated gluon distribution [70]. Forshaw, Sandapen and Shaw (FSS) [71] model the dipole-proton interaction through the exchange of a soft [56] and a hard [72] Pomeron, with (Sat) and without (Nosat) saturation, and use the DGKP and Gaussian ρ^0 wave-functions. In the model of Dosch and Ferreira (DF) [73], the dipole cross section is calculated using Wilson loops, making use of the stochastic vacuum model for the non-perturbative QCD contribution.

While the calculations based on two-gluon exchange are limited to relatively high-Q^2 values (typically ~4 GeV^2), those based on modelling the dipole cross section incorporate both the perturbative and non-perturbative aspects of ρ^0 production.

13.2 Comparison with data

The different predictions discussed above are compared to the Q^2 dependence of the cross section in Fig. 25. None of the models gives a good description of the data over the full kinematic range of the measurement. The FSS model with the three-dimensional Gaussian ρ^0 wave-function describes the low-Q^2 data very well, while the KMW and DF models describe the $Q^2 > 1$ GeV^2 region well.

The various predictions are also compared with the W dependence of the cross section, for different Q^2 values, in Fig. 26. Here again, none of the models reproduces the magnitude of the cross section measurements. The closest to the data, in shape and magnitude, are the MRT model with

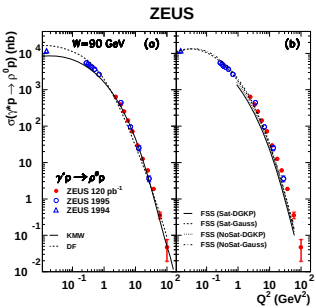

Figure 25
The Q^2 dependence of the $\gamma^* p \to \rho^0 p$ cross section at W = 90 GeV. The same data are plotted in (*a*) and (*b*), compared to different models, as described in the text. The predictions are plotted in the range as provided by the authors.

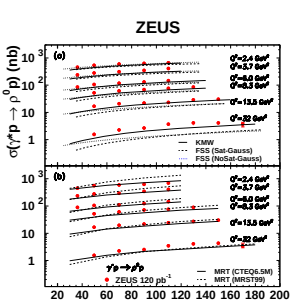

Figure 26
The W dependence of the $\gamma^* p \to \rho^0 p$ cross section for different values of Q^2, as indicated in the figure. The same data are plotted in (*a*) and (*b*), compared to different models, as described in the text. The predictions are plotted in the range as provided by the authors.

the CTEQ6.5M parametrisation of the gluon distribution in the proton and the KMW model. The KMW model gives a good description of the Q^2 dependence of δ as shown in Fig. 27.

The dependence of b on Q^2 is given only in the FKS and the KMW models as shown in Fig. 28. The FKS expectations are somewhat closer to the data.

The expected Q^2 dependence of r_{00}^{04} is compared to the measurements in Fig. 29. The MRT prediction, using the CTEQ6.5M gluon density, is the only prediction which describes the data in the whole Q^2 range. While all the models exhibit a mild dependence of r_{00}^{04} on W, consistent with the data as shown in Figs. 30 and 31, none of them reproduces correctly the magnitude of r_{00}^{04} in all the Q^2 bins.

In summary, none of the models considered above is able to describe all the features of the data presented in this paper. The high precision of the measurements can be used to refine models for exclusive ρ^0 electroproduction.

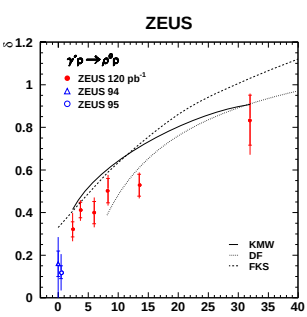

Figure 27
The value of δ from a fit of the form $\sigma \sim W^{\delta}$ for the reaction $\gamma^* p \to \rho^0 p$, as a function of Q^2. The lines are the predictions of models as denoted in the figure (see text).

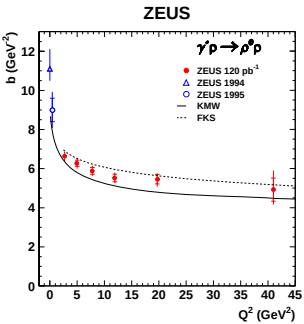

Figure 28
The value of the slope b from a fit of the form $d\sigma/d|t| \sim e^{-b|t|}$ for the reaction $\gamma^* p \to \rho^0 p$, as a function of Q^2. The lines are the predictions of models as denoted in the figure (see text).

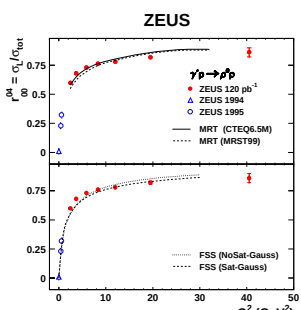

Figure 29
The ratio r_{00}^{04} as a function of Q^2 compared to the predictions of models as denoted in the figure (see text).

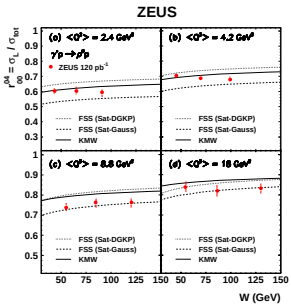

Figure 30

The ratio r_{00}^{04} as a function of W for different values of Q^2 compared to the predictions of models as indicated in the figure (see text).

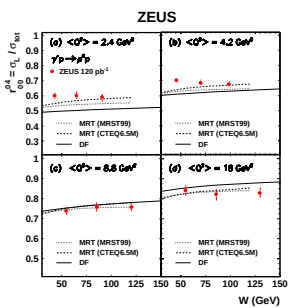

Figure 31

The ratio r_{00}^{04} as a function of W for different values of Q^2 compared to the predictions of models as indicated in the figure (see text).

14 Summary and Conclusion

Exclusive ρ^0 electroproduction has been studied by ZEUS at HERA in the range $2 < Q^2 < 160$ GeV^2 and $32 < W < 180$ GeV with a high statistics sample. The Q^2 dependence of the $\gamma^* p \to \rho^0 p$ cross section is a steeply falling function of Q^2. The cross section rises with W and its logarithmic derivative in W increases with increasing Q^2. The exponential slope of the t distribution decreases with increasing Q^2 and levels off at about $b = 5$ GeV^{-2}. The decay angular distributions of the ρ^0 indicate s-channel helicity breaking. The ratio of cross sections induced by longitudinally and transversely polarised virtual photons increases with Q^2, but is independent of W and of $|t|$, suggesting suppression of large-size configurations of the transversely polarised photon. The effective Pomeron trajectory, averaged over the full Q^2 range, has a larger intercept and a smaller slope than those extracted from soft interactions. All these features are compatible with expectations of perturbative QCD. However, none of the available models which have been compared to the measurements is able to reproduce all the features of the data.

The ZEUS Collaboration

S. Chekanov[1], M. Derrick, S. Magill, B. Musgrave, D. Nicholass[2], J. Repond, R. Yoshida

Argonne National Laboratory, Argonne, Illinois 60439-4815, USA [n]

M.C.K. Mattingly

Andrews University, Berrien Springs, Michigan 49104-0380, USA

M. Jechow, N. Pavel[†], A.G. Yagües Molina

Institut für Physik der Humboldt-Universität zu Berlin, Berlin, Germany [b]

S. Antonelli, P. Antonioli, G. Bari, M. Basile, L. Bellagamba, M. Bindi, D. Boscherini, A. Bruni, G. Bruni, L. Cifarelli, F. Cindolo, A. Contin, M. Corradi, S. De Pasquale, G. Iacobucci, A. Margotti, R. Nania, A. Polini, G. Sartorelli, A. Zichichi

University and INFN Bologna, Bologna, Italy [e]

D. Bartsch, I. Brock, H. Hartmann, E. Hilger, H.-P. Jakob, M. Jüngst, O.M. Kind[3], A.E. Nuncio-Quiroz, E. Paul[4], R. Renner[5], U. Samson, V. Schönberg, R. Shehzadi, M. Wlasenko

Physikalisches Institut der Universität Bonn, Bonn, Germany [b]

N.H. Brook, G.P. Heath, J.D. Morris

H.H. Wills Physics Laboratory, University of Bristol, Bristol, United Kingdom [m]

M. Capua, S. Fazio, A. Mastroberardino, M. Schioppa, G. Susinno, E. Tassi

Calabria University, Physics Department and INFN, Cosenza, Italy [e]

J.Y. Kim[6], K.J. Ma[7]

Chonnam National University, Kwangju, South Korea [g]

Z.A. Ibrahim, B. Kamaluddin, W.A.T. Wan Abdullah

Jabatan Fizik, Universiti Malaya, 50603 Kuala Lumpur, Malaysia [r]

Y. Ning, Z. Ren, F. Sciulli

Nevis Laboratories, Columbia University, Irvington on Hudson, New York 10027 [o]

J. Chwastowski, A. Eskreys, J. Figiel, A. Galas, M. Gil, K. Olkiewicz, P. Stopa, L. Zawiejski

The Henryk Niewodniczanski Institute of Nuclear Physics, Polish Academy of Sciences, Cracow, Poland [i]

L. Adamczyk, T. Bold, I. Grabowska-Bold, D. Kisielewska, J. Lukasik, M. Przybycień, L. Suszycki

Faculty of Physics and Applied Computer Science, AGH-University of Science and Technology, Cracow, Poland [p]

A. Kotański[8], W. Slomiński[9]

Department of Physics, Jagellonian University, Cracow, Poland

V. Adler[10], U. Behrens, I. Bloch, C. Blohm, A. Bonato, K. Borras, R. Ciesielski, N. Coppola, A. Dossanov, V. Drugakov, J. Fourletova, A. Geiser, D. Gladkov, P. Göttlicher[11], J. Grebenyuk, I. Gregor, T. Haas, W. Hain, C. Horn[12], A. Hüttmann, B. Kahle, I.I. Katkov, U. Klein[13], U. Kötz, H. Kowalski, E. Lobodzinska, B. Löhr, R. Mankel, I.-A. Melzer-Pellmann, S. Miglioranzi, A. Montanari, T. Namsoo, D. Notz, L. Rinaldi, P. Roloff, I. Rubinsky, R. Santamarta, U. Schneekloth, A. Spiridonov[14], H. Stadie, D. Szuba[15], J. Szuba[16], T. Theedt, G. Wolf, K. Wrona, C. Youngman, W. Zeuner

Deutsches Elektronen-Synchrotron DESY, Hamburg, Germany

W. Lohmann, S. Schlenstedt

Deutsches Elektronen-Synchrotron DESY, Zeuthen, Germany

G. Barbagli, E. Gallo, P. G. Pelfer

University and INFN Florence, Florence, Italy [e]

A. Bamberger, D. Dobur, F. Karstens, N.N. Vlasov[17]

Fakultät für Physik der Universität Freiburg i.Br., Freiburg i.Br., Germany [b]

P.J. Bussey, A.T. Doyle, W. Dunne, M. Forrest, D.H. Saxon, I.O. Skillicorn

Department of Physics and Astronomy, University of Glasgow, Glasgow, United Kingdom [m]

I. Gialas[18], K. Papageorgiu

Department of Engineering in Management and Finance, Univ. of Aegean, Greece

T. Gosau, U. Holm, R. Klanner, E. Lohrmann, H. Salehi, P. Schleper, T. Schörner-Sadenius, J. Sztuk, K. Wichmann, K. Wick

Hamburg University, Institute of Exp. Physics, Hamburg, Germany [b]

C. Foudas, C. Fry, K.R. Long, A.D. Tapper

Imperial College London, High Energy Nuclear Physics Group, London, United Kingdom [m]

M. Kataoka[19], T. Matsumoto, K. Nagano, K. Tokushuku[20], S. Yamada, Y. Yamazaki[21]

Institute of Particle and Nuclear Studies, KEK, Tsukuba, Japan [f]

A.N. Barakbaev, E.G. Boos, N.S. Pokrovskiy, B.O. Zhautykov

Institute of Physics and Technology of Ministry of Education and Science of Kazakhstan, Almaty, Kazakhstan

V. Aushev[1], M. Borodin, A. Kozulia, M. Lisovyi

Institute for Nuclear Research, National Academy of Sciences, Kiev and Kiev National University, Kiev, Ukraine

D. Son

Kyungpook National University, Center for High Energy Physics, Daegu, South Korea [g]

J. de Favereau, K. Piotrzkowski

Institut de Physique Nucléaire, Université Catholique de Louvain, Louvain-la-Neuve, Belgium [d]

F. Barreiro, C. Glasman[22], M. Jimenez, L. Labarga, J. del Peso, E. Ron, M. Soares, J. Terrón, M. Zambrana

Departamento de Física Teórica, Universidad Autónoma de Madrid, Madrid, Spain [l]

F. Corriveau, C. Liu, R. Walsh, C. Zhou

Department of Physics, McGill University, Montréal, Québec, Canada H3A 2T8 [a]

T. Tsurugai

Meiji Gakuin University, Faculty of General Education, Yokohama, Japan [f]

A. Antonov, B.A. Dolgoshein, V. Sosnovtsev, A. Stifutkin, S. Suchkov

Moscow Engineering Physics Institute, Moscow, Russia [j]

R.K. Dementiev, P.F. Ermolov, L.K. Gladilin, L.A. Khein, I.A. Korzhavina, V.A. Kuzmin, B.B. Levchenko[23], O.Yu. Lukina, A.S. Proskuryakov, L.M. Shcheglova, D.S. Zotkin, S.A. Zotkin

Moscow State University, Institute of Nuclear Physics, Moscow, Russia [k]

I. Abt, C. Büttner, A. Caldwell, D. Kollar, W.B. Schmidke, J. Sutiak

Max-Planck-Institut für Physik, München, Germany

G. Grigorescu, A. Keramidas, E. Koffeman, P. Kooijman, A. Pellegrino, H. Tiecke, M. Vázquez[19], L. Wiggers

NIKHEF and University of Amsterdam, Amsterdam, Netherlands [h]

N. Brümmer, B. Bylsma, L.S. Durkin, A. Lee, T.Y. Ling

Physics Department, Ohio State University, Columbus, Ohio 43210 [n]

P.D. Allfrey, M.A. Bell, A.M. Cooper-Sarkar, R.C.E. Devenish, J. Ferrando, B. Foster, K. Korcsak-Gorzo, K. Oliver, S. Patel, V. Roberfroid[24], A. Robertson, P.B. Straub, C. Uribe-Estrada, R. Walczak

Department of Physics, University of Oxford, Oxford United Kingdom [m]

P. Bellan, A. Bertolin, R. Brugnera, R. Carlin, F. Dal Corso, S. Dusini, A. Garfagnini, S. Limentani, A. Longhin, L. Stanco, M. Turcato

Dipartimento di Fisica dell' Università and INFN, Padova, Italy [e]

B.Y. Oh, A. Raval, J. Ukleja[25], J.J. Whitmore[26]

Department of Physics, Pennsylvania State University, University Park, Pennsylvania 16802 [o]

Y. Iga

Polytechnic University, Sagamihara, Japan [f]

G. D'Agostini, G. Marini, A. Nigro

Dipartimento di Fisica, Università 'La Sapienza' and INFN, Rome, Italy [e]

J.E. Cole, J.C. Hart

Rutherford Appleton Laboratory, Chilton, Didcot, Oxon, United Kingdom [m]

H. Abramowicz[27], R. Ingbir, S. Kananov, A. Kreisel, A. Levy, O. Smith, A. Stern

Raymond and Beverly Sackler Faculty of Exact Sciences, School of Physics, Tel-Aviv University, Tel-Aviv, Israel [d]

M. Kuze, J. Maeda

Department of Physics, Tokyo Institute of Technology, Tokyo, Japan [f]

R. Hori, S. Kagawa[28], N. Okazaki, S. Shimizu, T. Tawara

Department of Physics, University of Tokyo, Tokyo, Japan [f]

R. Hamatsu, H. Kaji[29], S. Kitamura[30], O. Ota, Y.D. Ri

Tokyo Metropolitan University, Department of Physics, Tokyo, Japan [f]

M.I. Ferrero, V. Monaco, R. Sacchi, A. Solano

Università di Torino and INFN, Torino, Italy [e]

M. Arneodo, M. Ruspa

Università del Piemonte Orientale, Novara, and INFN, Torino, Italy [e]

S. Fourletov, J.F. Martin

Department of Physics, University of Toronto, Toronto, Ontario, Canada M5S 1A7 [a]

S.K. Boutle[18], J.M. Butterworth, C. Gwenlan[31], T.W. Jones, J.H. Loizides, M.R. Sutton[31], M. Wing

Physics and Astronomy Department, University College London, London, United Kingdom [m]

B. Brzozowska, J. Ciborowski[32], G. Grzelak, P. Kulinski, P. Łużniak[33], J. Malka[33], R.J. Nowak, J.M. Pawlak, T. Tymieniecka, A. Ukleja, A.F. Żarnecki

Warsaw University, Institute of Experimental Physics, Warsaw, Poland

M. Adamus, P. Plucinski[34]

Institute for Nuclear Studies, Warsaw, Poland

Y. Eisenberg, I. Giller, D. Hochman, U. Karshon, M. Rosin

Department of Particle Physics, Weizmann Institute, Rehovot, Israel [c]

E. Brownson, T. Danielson, A. Everett, D. Kçira, D.D. Reeder[4], P. Ryan, A.A. Savin, W.H. Smith, H. Wolfe

Department of Physics, University of Wisconsin, Madison, Wisconsin 53706, USA [n]

S. Bhadra, C.D. Catterall, Y. Cui, G. Hartner, S. Menary, U. Noor, J. Standage, J. Whyte

Department of Physics, York University, Ontario, Canada M3J 1P3 [a]

[1] supported by DESY, Germany

[2] also affiliated with University College London, UK

[3] now at Humboldt University, Berlin, Germany

[4] retired

[5] self-employed

[6] supported by Chonnam National University in 2005

[7] supported by a scholarship of the World Laboratory Björn Wiik Research Project

[8] supported by the research grant no. 1 P03B 04529 (2005–2008)

[9] This work was supported in part by the Marie Curie Actions Transfer of Knowledge project COCOS (contract MTKD-CT-2004-517186)

[10] now at Univ. Libre de Bruxelles, Belgium

[11] now at DESY group FEB, Hamburg, Germany

[12] now at Stanford Linear Accelerator Center, Stanford, USA

[13] now at University of Liverpool, UK

[14] also at Institut of Theoretical and Experimental Physics, Moscow, Russia

[15] also at INP, Cracow, Poland

[16] on leave of absence from FPACS, AGH-UST, Cracow, Poland

[17] partly supported by Moscow State University, Russia

[18] also affiliated with DESY

[19] now at CERN, Geneva, Switzerland

[20] also at University of Tokyo, Japan

[21] now at Kobe University, Japan

[22] Ramón y Cajal Fellow

[23] partly supported by Russian Foundation for Basic Research grant no. 05-02-39028-NSFC-a

[24] EU Marie Curie Fellow

[25] partially supported by Warsaw University, Poland

[26] This material was based on work supported by the National Science Foundation, while working at the Foundation.

[27] also at Max Planck Institute, Munich, Germany, Alexander von Humboldt Research Award

[28] now at KEK, Tsukuba, Japan

[29] now at Nagoya University, Japan

[30] Department of Radiological Science

[31] PPARC Advanced fellow

[32] also at Łódź University, Poland

[33] Łódź University, Poland

[34] supported by the Polish Ministry for Education and Science grant no. 1 P03B 14129

[†] deceased

[a] supported by the Natural Sciences and Engineering Research Council of Canada (NSERC)

[b] supported by the German Federal Ministry for Education and Research (BMBF), under contract numbers 05 HZ6PDA, 05 HZ6GUA, 05 HZ6VFA and 05 HZ4KHA

[c] supported in part by the MINERVA Gesellschaft für Forschung GmbH, the Israel Science Foundation (grant no. 293/02-11.2) and the U.S.-Israel Binational Science Foundation

[d] supported by the German-Israeli Foundation and the Israel Science Foundation

[e] supported by the Italian National Institute for Nuclear Physics (INFN)

[f] supported by the Japanese Ministry of Education, Culture, Sports, Science and Technology (MEXT) and its grants for Scientific Research

[g] supported by the Korean Ministry of Education and Korea Science and Engineering Foundation

[h] supported by the Netherlands Foundation for Research on Matter (FOM)

[i] supported by the Polish State Committee for Scientific Research, grant no. 620/E-77/SPB/DESY/P-03/DZ 117/2003–2005 and grant no. 1P03B07427/2004–2006

[j] partially supported by the German Federal Ministry for Education and Research (BMBF)

[k] supported by RF Presidential grant N 8122.2006.2 for the leading scientific schools and by the Russian Ministry of Education and Science through its grant Research on High Energy Physics

[l] supported by the Spanish Ministry of Education and Science through funds provided by CICYT

[m] supported by the Particle Physics and Astronomy Research Council, UK

[n] supported by the US Department of Energy

[o] supported by the US National Science Foundation. Any opinion, findings and conclusions or recommendations expressed in this material are those of the authors and do not necessarily reflect the views of the National Science Foundation.

[p] supported by the Polish Ministry of Science and Higher Education as a scientific project (2006–2008)

[q] supported by FNRS and its associated funds (IISN and FRIA) and by an Inter-University Attraction Poles Programme subsidised by the Belgian Federal Science Policy Office

[r] supported by the Malaysian Ministry of Science, Technology and Innovation/Akademi Sains Malaysia grant SAGA 66-02-03-0048

Acknowledgements

It is a pleasure to thank the DESY Directorate for their strong support and encouragement. The remarkable achievements of the HERA machine group were essential for the successful completion of this work and are greatly appreciated. The design, construction and installation of the ZEUS detector has been made possible by the efforts of many people who are not listed as authors. We thank E. Ferreira, J. Forshaw, M. Strikman, T. Teubner and G. Watt, for providing the results of their calculations.

References

1. Abramowicz H, Caldwell A: *Rev Mod Phys* 1999, **71:**1275. This is an example reference.
2. Abramowicz H, Frankfurt L, Strikman M: *Surveys High Energy Phys* 1997, **11:**51.
3. Brodsky SJ, *et al.: Phys Rev D* 1994, **50:**3134.
4. ZEUS Coll, Breitweg J, *et al.: Phys Lett B* 2000, **487:**273.
5. ZEUS Coll, Chekanov S, *et al.: Nud Phys B* 2005, **718:**3.
6. ZEUS Coll, Chekanov S, *et al.: Nud Phys B* 2004, **695:**3.
7. H1 Coll, Adloff C, *et al.: Phys Lett B* 2000, **483:**360.
8. H1 Coll, Aktas A, *et al.: Eur Phys J C* 2006, **46:**585.
9. H1 Coll, Adloff C, *et al.: Eur Phys J C* 2000, **13:**371.
10. ZEUS Coll, Derrick M, *et al.: Eur Phys J C* 1999, **6:**603.
11. Collins JC, Frankfurt L, Strikman M: *Phys Rev D* 1997, **56:**2982.
12. Ivanov IP, Nikolaev NN, Savin AA: *Phys Part Nucl* 2006, **37:**1. This is an example reference.
13. Radyushkin AV: *Phys Rev D* 1997, **56:**5524.
14. Ji XD: *J Phys G* 1998, **24:**1181.
15. Frankfurt L, McDermott M, Strikman M: *JHEP* 2001, **103:**45.
16. Yu Ivanov D, Szymanowski L, Krasnikov G: *J Exp Theor Phys Lett* 2004, **80:**226.
17. McDermott MF: *The Dipole picture of small x physics: A Summary of the Amirim meeting, DESY-00-126* 2000.[arXiv: hep-ph/0008260]
18. Collins PDB: *An Introduction to Regge Theory and High Energy Physics* Cambridge University Press, Cambridge, England; 1977.
19. Cudell JR, Kang K, Kim S: *Phys Lett B* 1997, **395:**311.
20. Donnachie A, Landshoff PV: *Nucl Phys B* 1984, **231:**189.
21. H1 Coll, Adloff C, *et al.: Phys Lett B* 2001, **520:**183.
22. ZEUS Coll, Chekanov S, *et al.: Eur Phys J C* 2002, **24:**345.
23. ZEUS Coll, Holm U, (ed): *The ZEUS Detector, Status Report(unpublished), DESY* 1993 [http://www-zeus.desy.de/bluebook/bluebook.html].
24. ZEUS Coll, Derrick M, *et al.: Phys Lett B* 1992, **293:**465.
25. Harnew N, *et al.: Nucl Inst Meth A* 1989, **279:**290.
26. Foster B, *et al.: Nud Phys Proc Suppl B* 1993, **32:**181.
27. Foster B, *et al.: Nud Inst Meth A* 1994, **338:**254.
28. Derrick M, *et al.: Nud Inst Meth A* 1991, **309:**77.
29. Andersen A, *et al.: Nucl Inst Meth A* 1991, **309:**101.
30. Caldwell A, *et al.: Nud Inst Meth A* 1992, **321:**356.
31. Bernstein A, *et al.: Nucl Inst Meth A* 1993, **336:**33.
32. Bamberger A, *et al.: Nucl Inst Meth A* 1996, **382:**419.
33. Dwuraźny A, *et al.: Nud Inst Meth A* 1989, **277:**176.
34. Bamberger A, *et al.: Nucl Inst Meth A* 2000, **450:**235.
35. ZEUS Coll, Derrick M, *et al.: Z Phys C* 1997, **73:**253.
36. Andruszkow J, *et al.: First measurement of HERA luminosity by ZEUS lumi monitor, Preprint DESY-92-066, DESY* 1992.
37. ZEUS Coll, Derrick M, *et al.: Z Phys C* 1994, **63:**391.
38. Andruszkow J, *et al.: Acta Phys Pol B* 2001, **32:**2025.
39. ZEUS Coll, Derrick M, *et al.: Phys Lett B* 1995, **356:**601.
40. Beier H: *PhD thesis* Hamburg University, DESY Internal Report F35D-97-06; 1997.

41. Monteiro T: *PhD thesis* Hamburg University, DESY Internal Report DESYTHESIS-1998–027; 1998.
42. Kreisel A: *PhD thesis* Tel Aviv University, DESY Internal Report DESYTHESIS-2004–012; 2004.
43. Muchorowski K: *PhD thesis* Warsaw University; 1998.
44. Kwiatkowski A, Spiesberger H, Möhring H.-J: *Proceedings of the Workshop on Physics at HERA Volume III*. Edited by: Buchmueller W, Ingelman G. DESY, Hamburg; 1991:1294.
45. Kasprzak M: *PhD thesis* Warsaw University; 1995.
46. Sjöstrand T, *et al.*: *Comp Phys Comm* 2001, **135:**238.
47. Söding P: *Phys Lett B* 1966, **19:**702.
48. Particle Data Group, Yao W-M, *et al.*: *J Phys G* 2006, **33:**1.
49. Schilling K, Wolf G: *Nucl Phys B* 1973, **61:**381.
50. ZEUS Coll, Breitweg J, *et al.*: *Eur Phys J C* 2000, **12:**3.
51. Ivanov YuD, Kirschner R: *Phys Rev D* 1998, **58:**114026.
52. H1 Coll, Adloff C, *et al.*: *Phys Lett B* 2002, **539:**25.
53. ZEUS Coll, Breitweg J, *et al.*: *Eur Phys J C* 1998, **2:**2.
54. H1 Coll, Aktas A, *et al.*: *Eur Phys J C* 2005, **44:**1.
55. Ryskin MG, Shabelski Yu M: *Phys Atom Nucl* 1998, **61:**81, and correction in σ_L/σ_T in the ρ^0 meson diffractive electroproduction, [arXiv:hep-ph/9704279]
56. Donnachie A, Landshoff PV: *Phys Lett B* 1992, **296:**227.
57. Frankfurt L, Koepf W, Strikman M: *Phys Rev D* 1996, **54:**3194.
58. Frankfurt L, Koepf W, Strikman M: *Phys Rev D* 1998, **57:**512.
59. Martin AD, Ryskin MG, Teubner T: *Phys Rev D* 1997, **55:**4329.
60. Martin AD, Ryskin MG, Teubner T: *Phys Rev D* 2000, **62:**014022.
61. Martin AD, *et al.*: *Eur Phys J C* 1998, **4:**463.
62. CTEQ Coll, Tung WK, *et al.*: *JHEP* 2007, **0702:**053.
63. Kowalski H, Motyka L, Watt G: *Phys Rev D* 2006, **74:**074016.
64. Golec-Biernat K, Wuesthoff M: *Phys Rev D* 1999, **59:**014017.
65. Golec-Biernat K, Wuesthoff M: *Phys Rev D* 1999, **60:**114023.
66. Gribov VN, Lipatov LN: *Sov J Nucl Phys* 1972, **15:**438.
67. Lipatov LN: *Sov J Nucl Phys* 1975, **20:**94.
68. Altarelli G, Parisi G: *Nucl Phys B* 1977, **126:**298.
69. Dokshitzer Yu L: *Sov Phys JETP* 1977, **46:**298.
70. Kimber MA, Martin AD, Ryskin MG: *Phys Rev D* 2001, **63:**114027.
71. Forshaw JR, Sandapen R, Shaw G: *Phys Rev D* 2004, **69:**094013.
72. Donnachie A, Landshoff PV: *Phys Lett B* 2001, **518:**63.
73. Dosch HG, Ferreira E: *Euro Phys J C* 2007, **51:**83.